Title

State-averaged CASSCF with polarizable continuum model for studying photoreactions in solvents: Energies, analytical nuclear gradients, and non-adiabatic couplings

Journal

The Journal of Chemical Physics, 156(10)

ISSN

0021-9606

Author

Song, Chenchen

Publication Date

2022-03-14

DOI

10.1063/5.0085855

State-averaged CASSCF with polarizable continuum model for studying photoreactions in solvents: energies, analytical nuclear gradients and non-adiabatic couplings

Chenchen Song[1, a)]

Department of Chemistry, University of California Davis, Davis, CA 95616.

This paper presents state-averaged complete active space self-consistent field (SA-CASSCF) in polarizable continuum model (PCM) for studies of photoreactions in solvents. The wavefunctions of the solute and the PCM surface charges of the solvent are optimized simultaneously such that the state-averaged free energy is variationally minimized. The method supports both fixed weights as well as dynamic weights where the weights are automatically adjusted based on the energy gaps. The corresponding analytical nuclear gradients and non-adiabatic couplings are also derived. Furthermore, we show how the new method can be entirely formulated in terms of seven basic operations, which allows the implementation to benefit from existing high-performance libraries on grapical processing units (GPUs). Results demonstrating the accuracy and performance of the implementation are presented and discussed. We also apply the new method to the study of minimal conical intersection search and photoreaction energy pathways in solvents. Effects from the polarity of the solvents and different formula of dynamic weights are compared and discussed.

[a)]Electronic mail: ccsong@ucdavis.edu

I. INTRODUCTION

Photochemical processes taking place in solvent can be strongly affected by the properties of the solvents.[1] For example, experimental studies on stilbene have suggested that its fluorescence quantum yield has strong dependence on solvent viscosities.[2,3] Experimental studies on azobenzene have revealed that its long-time evolution is sensitive to solvent polarity but not to the viscosity.[4] A combination of theoretical and experimental studies on merocyanine have shown that its conical intersection can be tuned by the polarity of the solvent, achieving rational control of the excited state lifetime.[5,6]. Therefore, it's important to incorporate the solvation effects into the theoretical methods in order to properly simulate the photoreactions in solvents.

Although there have been substantial theoretical studies on solvation effects over the absorption and emission properties of organic molecules,[7,8] theoretical methods for studying photoreaction are much less mature. Due to the ultrafast and nonequilibrium nature of photoreactions and the important role played by the conical intersections,[9] theoretical studies of photoreactions in the gas phase generally involve locating the minimal energy conical intersections (MECIs)[10] and carrying out non-adiabatic molecular dynamics simulations.[11] Both types of simulations require analytical nuclear gradients and non-adiabatic coupling vectors. In order to apply similar studies to photoreactions in solvent, the primary goal of this work is to develop methods that can provide gradients and non-adiabatic couplings with solvation effects. In order to do this, we will first discuss what are the considerations for choosing the solvent model and electronic structure methods.

In terms of the solvent model for studying photoreactions, one of the main challenge is how to capture the time-dependent evolution of the solute-solvent interaction.[12] Upon exciting the solute molecule from ground to its excited state, the solvent polarization can be separated into the fast component from the electrons that respond immediately and the slow component from the nuclei that is frozen at its ground state equilibrium.[13,14] As the solute molecule propagates on the solvated excited states, the solvent electrons will continue to respond almost instantaneously while the solvent nuclei will gradually undergo vibrational relaxation. In addition to polarization effects, the dynamical properties of the nuclear motions such as viscosity will also affect the excited state dynamics of the solute as

shown by the examples discussed in the first paragraph.

Solvent models can generally be divided into implicit solvent models based on dielectric continuum approximation, and explicit solvent models that include solvent molecules directly. The implicit solvent models are advantageous in terms of their simplicity and that no sampling of solvent configurations is required. Polarizable continuum model (PCM)[15] along with its conductor-like variants[16,17] are among the most popular implicit solvent models. Such models primarily capture the polarization of the solvent, and leave out interactions related to solvent nuclear configurations (e.g. hydrogen bonding) and nuclear dynamics (e.g. viscosity). Although time-dependent PCM has been reported,[12,18] PCM with constant dielectric constant is still more widely implemented in quantum chemistry software at the moment. The latter is most suitable for studying photoreactions in non-polar organic solvents where the polarization is dominated by the electrons. In contrast, all explicit solvent models require configuration samplings, but can provide more atomistic details. Quantum chemical (QM) explicit solvent certainly captures the most physics, but is impratical for most studies due to its extremely high computational cost. Classical explicit solvent model using fixed charge force fields[8,19–21] can capture solute-solvent interactions related to the the nuclear configurations and dynamics, but the fixed charges make it unable to describe the fast response of the solvent electrons. Classical solvents using polarizable force fields[22–25] improve on this by introducing a set of polarizable induced dipoles reflecting the fast response of the solvent electrons, making it particularly appealing for studying photoreactions.[26] Based on the above considerations, we will focus on PCM with constant dielectric constant as an initial step, and we anticipate that a lot of the discussions in this work can be generalized to polarizable forcefield in the future due to their similarities in treating the polarizable parameters.

In terms of choosing the electronic structure methods for describing the excited solute, the most important considerations for this work are the differentiability of the method and the ability to properly describe the conical intersections. Linear response time-dependent density functional theory (TDDFT)[27,28] are not suitable because they do not correctly describe the topology of conical intersections between ground and excited states,[29] and multi-reference methods are more appropriate for carrying out excited state dynamics simulations.[30] However, compared to TDDFT where the ground and excited state calculations are independent, adding polarizable solvent model to multi-state multi-reference methods is much less straight-

forward. For the purpose of studying photoreactions, Hagras et al. recently compared different ways of incorporating polarizable models,[31] and divided the existing works into three categories: reference state approach[32] (including linear response approach[33,34]), state-specific approach,[35,36] and state-averaged approach[37]. We refer the readers to their work for detailed discussions regarding the pros and cons for each approach. Of the three, only the state-averaged approach is able to properly describe the conical intersections. However, it lacks the ability to capture different solvent responses to each electronic states, resulting in worse descriptions near the Franck-Condon region. To remedy this, one method is to add perturbative specific corrections to the state-averaged results,[37] but we decided not to pursue this route because it makes the development of both nuclear gradient and non-adiabatic couplings more complicated. Another method is to use a dynamically weighted (DW) scheme[38–40] based on the energy differences from the reference state. This allows assigning more weights to the state of interests near the Franck-Condon region, while approaching equally-weighted state-averaged description towards the conical intersections.[31] Furthermore, both analytical gradients and non-adiabatic couplings for state-averaged CASSCF[41–43] with dynamic weights have been developed recently for gas-phase calculations.[44] Based on the these considerations, we develop SA-CASSCF in PCM with supports for both fixed weights as well as dynamic weights, and develop the corresponding analytical gradients and non-adiabatic couplings.

Because multi-reference methods are generally more expensive compared to single reference methods, performance of the implementation is another factor that often limits the systems that can be simulated. Recently, Hohenstein et.al[45] reported an atomic-orbital formulation of SA-CASSCF by reformulating the entire method in terms of Fock builds to benefit from the highly-optimized integral libraries on the graphical processing units (GPUs).[46–48] Snyder et al. generalized this idea and shown that the corresponding analytical gradients and non-adiabatic couplings can also be reformulated in terms of Fock builds and Fock gradients.[49,50] These works suggested that high performance implementation of a new method can be enabled by formulating electronic structure methods in terms of existing well-defined GPU kernels.

Following the above discussions, in this work we develop dynamically weighted SA-CASSCF in PCM for the purpose of studying excited state dynamics in solvents, including energies, analytical nuclear gradients and non-adiabatic couplings. In particular, the

new method is formulated in terms of established GPU kernels to benefit the performance. To our knowledge this is the first implementation of analytical gradients and non-adiabatic couplings for this level of theory, and enables the optimization of conical intersections in continuum solvent for the first time. This paper is structured as follows. In Section II, we will start by providing the list of basic operations of GPU kernels needed in this work. In Sections II A through II C, the energies, analytical nuclear gradients and non-adiabatic couplings for equal weights SA-CASSCF in PCM will be discussed respectively. In Section II D, generalization to dynamically weighted SA-CASSCF will be discussed. In each of these subsections, we will first briefly summarize the main ideas of the atomic-orbital formulated SA-CASSCF, and then show how the gas-phase equations can be extended when PCM is incorporated. Results from accuracy and performance testings as well as studies of model systems will be presented in Section III.

The indices and conventions used throughout this paper are summarized as follows.

- Φ: determinant index
- CASSCF state indices: Θ and Π are the target states; R, S are arbitrary states; I, J are internal states; A, B are external states.
- Molecular orbital (MO) indices: p, q, r, s are arbitrary MOs; i, j are closed orbitals; t, u are active orbitals; a, b are virtual orbitals. σ is spin.
- N is nuclear charge index and ξ is nuclear coordinate index.
- n, m : PCM surface charge indices.
- A vector or matrix will either be written with all indices (e.g. P_{pq}) or written in bold without indices (e.g. $\mathbf{P}$). Superscripts in paranthesis are generally used to denote different quantities of similar properties, such as $\mathbf{g}^{(\text{block1})}$ versus $\mathbf{g}^{(\text{block2})}$.
- Tilde denotes a function call, and the square bracket indicates input variables (see Eq.2 as example).

II. METHOD

Generally, the free energy of a system with solvation described by PCM surface charges (denoted as q_n) can be written as

$$G = E^{\text{System}} + \sum_{pqn} P_{pq}\beta_{pq,n}q_n + \sum_{Nn} Z_N B_{N,n} q_n + \frac{1}{2}\sum_{mn} q_m A_{mn} q_n \tag{1}$$

The second and third terms in Eq.1 represent the interaction between the system and the surface charges, where P_{pq} and Z_N denote the electronic density and nuclear charges respectively. The last term represents the interaction between the surface charges. The expressions for $\beta_{pq,n}$,B_{Nn} and A_{mn} depend on the specific PCM model. In this work, we used the conductor-like polarizable continuum model[16,51] with switching Gaussian smooth discretization,[52,53] as implemented on GPU by Liu et al.[54,55]

As discussed in the introduction, we will formulate the new method in terms of the existing GPU kernels for performance improvements. The GPU kernels needed for this work are summarized below:

(1) Given a set of surface charges $\mathbf{q}$, compute the corresponding potential on the electrons

$$\tilde{V}_{pq}[\mathbf{q}] = \sum_{n} \beta_{pq,n} q_n \tag{2}$$

(2) Given a density matrix $\mathbf{P}$, compute the corresponding potential on the surface charges

$$\tilde{U}_{n}[\mathbf{P}] = \sum_{pq} P_{pq}\beta_{pq,n} \tag{3}$$

(3) Given a density matrix $\mathbf{P}$ and a set of surface charges $\mathbf{q}$, compute the nuclear gradients of the interaction energy:

$$\tilde{\beta}_{\xi}[\mathbf{P},\mathbf{q}] = \sum_{pq,n} P_{pq}\frac{\partial \beta_{pq,n}}{\partial \xi} q_n \tag{4}$$

(4) Given a set of nuclear charges $\mathbf{Z}$ and surface charges $\mathbf{q}$, compute the nuclear gradients of the interaction energy:

$$\tilde{B}_\xi[\mathbf{Z}, \mathbf{q}] = \sum_{N,n} Z_N \frac{\partial B_{N,n}}{\partial \xi} q_n \tag{5}$$

(5) Given two sets of surface charges $\mathbf{q}$ and $\mathbf{q}'$, compute the nuclear gradients of the interaction energy:

$$\tilde{A}_\xi[\mathbf{q}, \mathbf{q}'] = \sum_{mn} q_m \frac{\partial A_{mn}}{\partial \xi} q'_n \tag{6}$$

In addition to the PCM related operations, two additional operations are needed for contracting CASSCF wavefunctions (i.e. CI vectors) as implemented by Fales et al.[56]:

(6) Given two CI vectors c_Φ and $c'_{\Phi'}$, compute the one particle density matrix:

$$\tilde{\gamma}_{rs}[\mathbf{c}, \mathbf{c}'] = \sum_{\Phi\Phi'\sigma} c_\Phi \langle \Phi | a^\dagger_{r\sigma} a_{s\sigma} | \Phi' \rangle c'_{\Phi'} \tag{7}$$

(7) Given a CI vector c_Φ and a one-electron operator h_{tu} in the active space, apply the operator to the CI vector

$$\tilde{z}_\Phi[\mathbf{h}, \mathbf{c}] = \sum_{rs\sigma\Phi'} h_{rs} \langle \Phi | a^\dagger_{r\sigma} a_{s\sigma} | \Phi' \rangle c_{\Phi'} \tag{8}$$

In the following discussions, we will start with describing how PCM is incorporated into fixed-weights SA-CASSCF using the above operations, where energies, analytical nuclear gradients and non-adiabatic couplings are discussed in Sections II A, II B and II C respectively. In Section II D, we will discuss additional terms needed to enable PCM support for dynamic weighted SA-CASSCF.

A. Energy

In the gas phase, SA-CASSCF involves variationally minimizing the following objective function

$$E^{(\mathrm{SA})} = \sum_I w_I E_I = \sum_{pq} P^{(\mathrm{SA})}_{pq} h_{pq} + \sum_{pqrs} \Pi^{(\mathrm{SA})}_{pqrs} (pq|rs) \tag{9}$$

and convergence is reached when MO and CI coefficients satisfy

$$\frac{\partial E^{(\mathrm{SA})}}{\partial \kappa_{rs}} = 0, \frac{\partial E^{(\mathrm{SA})}}{\partial \theta_{RS}} = 0 \tag{10}$$

In the above equations, w_I represent weights, $\mathbf{P}^{(\mathrm{SA})}$ and $\mathbf{\Pi}^{(\mathrm{SA})}$ represent the state-averaged one-particle and two-particle density matrices, h_{pq} represents one-electron integrals (i.e. kinetic and nuclear attraction integrals), and $(pq|rs)$ represents two-electron repulsion integrals. κ_{rs} represents unitary rotations between molecular orbitals, and θ_{RS} represents unitary rotations between CI vectors. The algorithm implemented by Hohenstein et al.[45] in the atomic orbital formulated SA-CASSCF is outlined in Table I, which is a type of first-order orbital optimization algorithm that updates the CI and MO coefficients in alternating steps. Optimization of the MO coefficients requires the gradients of the objective function with respect to the orbital rotations

$$g_{rs}^{(\mathrm{O;SA})} = \frac{\partial E^{(\mathrm{SA})}}{\partial \kappa_{rs}} = \frac{\partial}{\partial \kappa_{rs}} \left(\sum_{pq} P_{pq}^{(\mathrm{SA})} h_{pq} + \sum_{pqrs} \Pi_{pqrs}^{(\mathrm{SA})} (pq|rs) \right) \tag{11}$$

If Newton-Raphson optimization is used, the MO coefficients are rotated by $\delta\kappa_{rs} = -H_{rs,rs}^{-1} g_{rs}^{(\mathrm{O;SA})}$. The Hessian may be approximated using only the diagonal elements. Other optimization algorithms can be applied here, such as the trust region algorithm[57] that increases the Hessian elements uniformly to restrict the step size. With the new MO coefficients, the CI coefficients $c_{I\Phi}$ are then updated by diagonalizing the Hamiltonian.

When PCM is included, the objective function is modified as

$$E^{(\text{SA-PCM})} = E^{(\mathrm{SA})} + \Delta^{(\text{SA-PCM})} \tag{12}$$

where $E^{(\mathrm{SA})}$ is same as Eq.9, and $\Delta^{(\text{SA-PCM})}$ is defined based on the last three terms in Eq.1

$$\Delta^{(\text{SA-PCM})} = \sum_{pqn} P_{pq}^{(\mathrm{SA})} \beta_{pq,n} q_n + \sum_{Nn} Z_N B_{N,n} q_n + \frac{1}{2} \sum_{mn} q_m A_{mn} q_n \tag{13}$$

The MO coefficients, CI coefficients and surface charges are solved variationally such that the following three criteria are all satisfied:

$$\frac{\partial E^{(\text{SA-PCM})}}{\partial \kappa_{rs}} = 0, \frac{\partial E^{(\text{SA-PCM})}}{\partial \theta_{RS}} = 0, \frac{\partial E^{(\text{SA-PCM})}}{\partial q_n} = 0 \tag{14}$$

Previous works on MCSCF in PCM[58] go back and forth between optimizing the wavefunction and updating the surface charges to be in equilibrium with the wavefunction. We think this approach is not straightforward to incorporate into the existing framework shown in Table I, since changing either the MO or the CI coefficients will both result in that the surface charges are no longer in equilibrium with the current wavefunction. Instead, we take a different strategy and treat the MO coefficients and PCM surface charges on the same footing.

Following the gas phase algorithm, we need the gradients of the objective function $\frac{\partial E^{(\text{SA-PCM})}}{\partial \kappa_{rs}}$ and $\frac{\partial E^{(\text{SA-PCM})}}{\partial q_n}$. From Eq.9 and Eq.13, one can show that

$$g_{rs}^{(\text{O;SA-PCM})} = \frac{\partial E^{(\text{SA-PCM})}}{\partial \kappa_{rs}} = \frac{\partial}{\partial \kappa_{rs}} \left(\sum_{pq} P_{pq}^{(\text{SA})} \eta_{pq} + \sum_{pqrs} \Pi_{pqrs}^{(\text{SA})} (pq|rs) \right) \tag{15}$$

$$\eta_{pq} = h_{pq} + \tilde{V}_{pq} \left[\mathbf{q} \right] \tag{16}$$

where the operation $\tilde{V}$ is defined in Eq.2. This suggests that the MO coefficients can be optimized with the existing gas phase codes by simply replacing h_{pq} with η_{pq}. To compute $\frac{\partial E^{(\text{SA-PCM})}}{\partial q_n}$, note that $E^{(\text{SA})}$ has no dependence on q_n. Thus from Eq.13, we have

$$g_n^{(\text{Q;SA-PCM})} = \frac{\partial E^{(\text{SA-PCM})}}{\partial q_n} = \tilde{U}_n[\mathbf{P}^{(\text{SA})}] + \sum_N Z_N B_{N,n} + \sum_m q_m A_{mn} \tag{17}$$

where $\tilde{U}$ represents the GPU kernel in Eq.3. To optimize the surface charges with Newton-Raphson algorithm, we neglect the off-diagonal Hessian components between the surface charges and MO rotations. This leads to

$$\delta \mathbf{q} = -\mathbf{A}^{-1} \cdot \mathbf{g}^{(\text{Q;SA-PCM})} \tag{18}$$

which is equivalent to

$$\mathbf{A} \cdot \delta \mathbf{q} = -\mathbf{g}^{(\text{Q;SA-PCM})} \tag{19}$$

This suggests that $\delta \mathbf{q}$ can be computed by solving the above linear system using the pre-conditioned conjugate gradient solver already implemented in Liu et al.[55]

From the above discussions, Eq.16, Eq.17 and Eq.19 are all that are needed to incorporate

PCM in to SA-CASSCF energy calculations. The algorithm is summarized in Table I, where the right column shows the additional operations from including PCM.

B. Analytical nuclear gradients

Methods for computing the analytical gradients of single state CASSCF in PCM have already been developed by Cossi et al.[58] When multiple states are included, the analytical gradients are more complicated and solving the coupled-perturbed equation is required.[59,60] The algorithm for atomic orbital formulated SA-CASSCF analytical gradients in the gas phase is summarized in the left column of Table II, which follows the works of Snyder et.al..[49,50] After getting necessary variables from the energy calculations, the algorithm can be divided into two parts: solving the coupled perturbed equation to obtain the Lagrange multipliers, and constructing the effective density matrices for contraction with the nuclear gradients of integrals. Below, we will show how these steps are generalized when PCM is included.

1. Coupled perturbed equation

In the gas phase, the analytical nuclear gradient calculations evaluate the nuclear derivatives of the target state energy

$$E_\Theta = \sum_{pq} P^\Theta_{pq} h_{pq} + \sum_{pqrs} \Pi^\Theta_{pqrs} (pq|rs) + \epsilon^{(\text{nuclei})} \tag{20}$$

where P^Θ_{pq} and Π^Θ_{pqrs} are the one electron and two electron density matrices for state Θ, and $\epsilon^{(\text{nuclei})}$ represents the nuclear repulsion energy. Using the Lagrange multiplier method,[59] the nuclear derivatives $\frac{dE_\Theta}{d\xi}$ is equal to the partial derivatives of the Lagrangian $\frac{\partial L_\Theta}{\partial \xi}$, which is defined by including E_Θ and the constraints for MO and CI coefficients from Eq.10

$$L^{(\text{SA})}_\Theta = E_\Theta + \sum_{pq} \bar{\kappa}^\Theta_{pq} \frac{\partial E^{(\text{SA})}}{\partial \kappa_{pq}} + \sum_{RS} \bar{\theta}^\Theta_{RS} \frac{\partial E^{(\text{SA})}}{\partial \theta_{RS}} \tag{21}$$

The Lagrange multipliers $\bar{\kappa}^{\Theta}_{pq}$ and $\bar{\theta}^{\Theta}_{RS}$ are solved by requiring that

$$\frac{\partial L^{(\mathrm{SA})}_{\Theta}}{\partial \kappa_{pq}} = 0, \frac{\partial L^{(\mathrm{SA})}_{\Theta}}{\partial \theta_{RS}} = 0 \tag{22}$$

This leads to the coupled perturbed equation for SA-CASSCF in the gas phase as

$$\begin{pmatrix} \mathbf{H}^{(\mathrm{OO})} & \mathbf{H}^{(\mathrm{OC})} \\ \mathbf{H}^{(\mathrm{CO})} & \mathbf{H}^{(\mathrm{CC})} \end{pmatrix} \begin{pmatrix} \bar{\boldsymbol{\kappa}}^{\Theta} \\ \bar{\boldsymbol{\theta}}^{\Theta} \end{pmatrix} = \begin{pmatrix} -\mathbf{g}^{(\mathrm{O}),\Theta} \\ \mathbf{0} \end{pmatrix} \tag{23}$$

In Eq.23, (O) and (C) indicate terms related to MO and CI rotations respectively. The Hessian matrix $\mathbf{H}$ is defined as $\frac{\partial E^{(\mathrm{SA})}}{\partial \alpha \partial \beta}$,where α, β can be κ_{pq} or θ_{RS}. On the right hand side, we have

$$g^{(\mathrm{O}),\Theta}_{rs} = \frac{\partial E_{\Theta}}{\partial \kappa_{rs}} = \frac{\partial}{\partial \kappa_{rs}} \left(\sum_{pq} P^{\Theta}_{pq} h_{pq} + \sum_{pqrs} \Pi^{\Theta}_{pqrs} (pq|rs) \right) \tag{24}$$

When only keeping the non-redundant contributions in the coupled perturbed equations, $\bar{\boldsymbol{\kappa}}^{\Theta}$ is composed of $\bar{\kappa}^{\Theta}_{iu}$, $\bar{\kappa}^{\Theta}_{ia}$ and $\bar{\kappa}^{\Theta}_{ua}$. $\bar{\boldsymbol{\theta}}^{\Theta}$ consists of rotations between pairs of internal states with unequal weights $\bar{\theta}^{\Theta}_{IJ,(w_I \neq w_J)}$ and rotations between internal and external states $\bar{\theta}^{\Theta}_{IA}$. However, because it's difficult to solve for all external states when the active space is large, Snyder et.al proposed a direct-compatible solver by replacing $\bar{\theta}^{\Theta}_{IA}$ with $\bar{c}^{\Theta}_{I\Phi}$,[50] where $\bar{c}^{\Theta}_{I\Phi}$ is the Lagrange multiplier corresponding to $\frac{\partial E^{(\mathrm{SA})}}{\partial c_{I\Phi}}$. Both situations will be considered in the discussions of PCM below.

When PCM is included, the target state energy is modified as

$$E^{(\mathrm{PCM})}_{\Theta} = E_{\Theta} + \Delta^{(\mathrm{PCM})}_{\Theta} \tag{25}$$

where

$$\Delta^{(\mathrm{PCM})}_{\Theta} = \sum_{pqn} P^{\Theta}_{pq} \beta_{pq,n} q_n + \sum_{Nn} Z_N B_{N,n} q_n + \frac{1}{2} \sum_{mn} q_m A_{mn} q_n \tag{26}$$

The corresponding Lagrangian is then defined by including the constraints from Eq.14

$$L_{\Theta}^{(\text{SA-PCM})} = E_{\Theta}^{(\text{PCM})} + \sum_{pq} \bar{\kappa}_{pq}^{\Theta} \frac{\partial E^{(\text{SA-PCM})}}{\partial \kappa_{pq}} + \sum_{RS} \bar{\theta}_{RS}^{\Theta} \frac{\partial E^{(\text{SA-PCM})}}{\partial \theta_{RS}} + \sum_{n} \bar{q}_{n}^{\Theta} \frac{\partial E^{(\text{SA-PCM})}}{\partial q_n} \quad (27)$$

The three types of Lagrange multipliers $\bar{\boldsymbol{\kappa}}$, $\bar{\boldsymbol{\theta}}$ and $\bar{\mathbf{q}}$ are determined simultaneously by

$$\frac{\partial L_{\Theta}^{(\text{SA-PCM})}}{\partial \kappa_{pq}} = 0, \frac{\partial L_{\Theta}^{(\text{SA-PCM})}}{\partial \theta_{RS}} = 0, \frac{\partial L_{\Theta}^{(\text{SA-PCM})}}{\partial q_n} = 0 \quad (28)$$

This leads to the following coupled perturbed equation for SA-CASSCF in PCM:

$$\begin{pmatrix} \mathbb{H}^{(\text{OO})} & \mathbb{H}^{(\text{OC})} & \mathbb{H}^{(\text{OQ})} \\ \mathbb{H}^{(\text{CO})} & \mathbb{H}^{(\text{CC})} & \mathbb{H}^{(\text{CQ})} \\ \mathbb{H}^{(\text{QO})} & \mathbb{H}^{(\text{QC})} & \mathbb{H}^{(\text{QQ})} \end{pmatrix} \begin{pmatrix} \bar{\boldsymbol{\kappa}}^{\Theta} \\ \bar{\boldsymbol{\theta}}^{\Theta} \\ \bar{\mathbf{q}}^{\Theta} \end{pmatrix} = \begin{pmatrix} -\mathbf{g}^{(\text{O;PCM}),\Theta} \\ \mathbf{0} \\ -\mathbf{g}^{(\text{Q;PCM}),\Theta} \end{pmatrix} \quad (29)$$

In Eq.29, the Hessian is defined as $\mathbb{H}_{\alpha\beta} = \frac{\partial^2 E^{(\text{SA-PCM})}}{\partial \alpha \partial \beta}$ where α, β can be κ_{pq},θ_{RS} or q_n. The right hand side contains the orbital and charge gradients of the target state energy. Similar to the derivations of Eq.15, one can show that $\mathbf{g}^{(\text{O;PCM}),\Theta}$, $\mathbb{H}^{(\text{OO})}$, $\mathbb{H}^{(\text{OO})}$,$\mathbb{H}^{(\text{OO})}$ and $\mathbb{H}^{(\text{OO})}$ can all be evaluated using the gas phase codes by replacing h_{pq} with η_{pq} defined in Eq.16. The following discussion will focus on the other terms unique to PCM.

To compute the charge gradients of the target state, similar to Eq.17, we have

$$g_n^{(\text{Q;PCM}),\Theta} = \frac{\partial \Delta_{\Theta}^{(\text{PCM})}}{\partial q_n} = \tilde{U}_n[\mathbf{P}^{\Theta}] + \sum_{N} Z_N B_{N,n} + \sum_{m} q_m A_{mn} \quad (30)$$

To evaluate the Hessian elements evolving surface charges, by taking derivatives of $\mathbf{g}^{(\text{Q;SA-PCM})} = \frac{\partial E^{(\text{SA-PCM})}}{\partial q_n}$ in Eq.17, one can show that

$$\mathbb{H}_{mn}^{(\text{QQ})} = A_{mn} \quad (31)$$

$$\mathbb{H}_{pq,n}^{(\text{OQ})} = \mathbb{H}_{n,pq}^{(\text{QO})} = 2 \sum_{r} P_{rp}^{(\text{SA})} \beta_{rq,n} - 2 \sum_{r} P_{rq}^{(\text{SA})} \beta_{rp,n} \quad (32)$$

For CI block corresponding to θ_{IJ},

$$\mathbb{H}^{(\mathrm{CQ})}_{IJ,n} = \mathbb{H}^{(\mathrm{QC})}_{n,IJ} = 2\left(w_I - w_J\right)\sum_{rs} T^{IJ}_{rs}\beta_{rs,n} \tag{33}$$

where $\mathbf{T}^{IJ}$ is the transition density matrix, and can be computed with operation in Eq.7 as $T^{IJ}_{rs} = \tilde{\gamma}_{rs}[\mathbf{c}_I, \mathbf{c}_J]$. For the CI block corresponding to the internal-external rotations, if the active space is small, the Hessian is defined with respect to θ_{IA}

$$\mathbb{H}^{(\mathrm{CQ})}_{IA,n} = \mathbb{H}^{(\mathrm{QC})}_{n,IA} = 2w_I\sum_{rs} T^{IA}_{rs}\beta_{rs,n} \tag{34}$$

If the active space is large, then the Hessian is defined with respect to $c_{I\Phi}$

$$\mathbb{H}^{(\mathrm{CQ})}_{I\Phi,n} = \mathbb{H}^{(\mathrm{QC})}_{n,I\Phi} = 2w_I\sum_{rs\sigma\Phi'} \langle\Phi|a^\dagger_{r\sigma}a_{s\sigma}|\Phi'\rangle c_{I\Phi'}\cdot\beta_{rs,n} \tag{35}$$

Because the number of PCM surface charges is often much larger than the number of basis functions, explicitly storing the matrix elements of Hessian from Eq.32 to Eq.35 is impractical for large molecules. Fortunately, the coupled-perturbed equations are solved iteratively, which mainly requires the matrix-vector product between the Hessian and the trial vector $\boldsymbol{\sigma} = \mathbb{H}\cdot\mathbf{v}$. This allows us to develop a direct formulation, which doesn't require the storage of any matrix elements from Eq.32 to Eq.35 as described below.

Given a trial vector $\bar{\mathbf{q}}$, in order to compute the additional contributions to $\boldsymbol{\sigma}^{(\mathrm{O})}$ from $\mathbb{H}^{(\mathrm{OQ})}\cdot\bar{\mathbf{q}}$ and the addition contributions to $\boldsymbol{\sigma}^{(\mathrm{C})}$ from $\mathbb{H}^{(\mathrm{CQ})}\cdot\bar{\mathbf{q}}$, we first compute

$$\bar{V}_{pq} = \tilde{V}_{pq}[\bar{\mathbf{q}}] \tag{36}$$

Based on Eq.32, the contribution from $\mathbb{H}^{(\mathrm{OQ})}\cdot\bar{\mathbf{q}}$ can then be computed as

$$\sigma^{(\mathrm{O})}_{pq} \mathrel{+}= 2\sum_r P^{(\mathrm{SA})}_{rp}\bar{V}_{rq} - 2\sum_r P^{(\mathrm{SA})}_{rq}\bar{V}_{rp} \tag{37}$$

More specifically, the non-redundant components are:

$$\sigma^{(\mathrm{O})}_{iu} \mathrel{+}= 4\bar{V}_{iu} - 2\sum_t P^{(\mathrm{SA})}_{tu}\cdot\bar{V}_{ti} \tag{38}$$

$$\sigma_{ia}^{(\mathrm{O})} \mathrel{+}= 4\bar{V}_{ia} \tag{39}$$

$$\sigma_{ua}^{(\mathrm{O})} \mathrel{+}= 2\sum_{t} P_{tu}^{(\mathrm{SA})} \cdot \bar{V}_{ta} \tag{40}$$

From Eq.33, the contributions from $\sum_n \mathbb{H}_{IJ,n}^{(\mathrm{OO})} \bar{q}_n$ can be computed as

$$\sigma_{IJ}^{(\mathrm{C})} \mathrel{+}= 2(w_I - w_J) \sum_{rs} T_{rs}^{IJ} \cdot \bar{V}_{rs} \tag{41}$$

For small active space, based on Eq.34, the contributions from $\sum_n \mathbb{H}_{IA,n}^{(\mathrm{OO})} \bar{q}_n$ can be computed as

$$\sigma_{IA}^{(\mathrm{C})} \mathrel{+}= 2w_I \sum_{rs} T_{rs}^{IA} \cdot \bar{V}_{rs} \tag{42}$$

For large active space, based on Eq.35, the contributions from $\sum_n \mathbb{H}_{I\Phi,n}^{(\mathrm{OO})} \bar{q}_n$ can be computed as

$$\sigma_{I\Phi}^{(\mathrm{C})} \mathrel{+}= 2w_I \sum_{rs\sigma\Phi'} \langle \Phi | a_{r\sigma}^{\dagger} a_{s\sigma} | \Phi' \rangle c_{I\Phi'} \cdot \bar{V}_{rs} = 2w_I \cdot \tilde{z}_{\Phi}[\bar{\mathbf{V}}, \mathbf{c}_I] \tag{43}$$

where we have used the operation defined in Eq.8.

To compute $\sigma^{(\mathrm{Q})} = \mathbb{H}^{(\mathrm{QO})} \cdot \bar{\boldsymbol{\kappa}} + \mathbb{H}^{(\mathrm{QC})} \cdot \bar{\boldsymbol{\theta}} + \mathbb{H}^{(\mathrm{QQ})} \cdot \bar{\mathbf{q}}$, we formulate the results in the form of

$$\sigma_n^{(\mathrm{Q})} = \sum_m A_{mn} \bar{q}_m + \tilde{U}_n[\bar{\mathbf{D}}] \tag{44}$$

where the first term comes from Eq.31, and $\bar{D}_{pq}$ in the second term contains contributions from trial vectors $\bar{\boldsymbol{\kappa}}$ and $\bar{\boldsymbol{\theta}}$. Based on Eq.32, contributions to $\bar{D}_{pq}$ from $\bar{\kappa}_{pq}$ are

$$\bar{D}_{iu} \mathrel{+}= 4\bar{\kappa}_{iu} - 2\sum_{t} P_{ut}^{(\mathrm{SA})} \bar{\kappa}_{it} \tag{45}$$

$$\bar{D}_{ia} \mathrel{+}= 4\bar{\kappa}_{ia} \tag{46}$$

$$\bar{D}_{ua} \mathrel{+}= 2\sum_{t} P^{(\mathrm{SA})}_{tu}\bar{\kappa}_{ta} \tag{47}$$

Based on Eq.33, additional contributions to $\bar{D}_{pq}$ from $\bar{\theta}_{IJ}$ are

$$\bar{D}_{rs} \mathrel{+}= \sum_{IJ} 2(w_I - w_J)\cdot T^{IJ}_{rs}\bar{\theta}_{IJ} \tag{48}$$

Depending on the active space size, based on Eq.34 or Eq.35, additional contributions to $\bar{D}_{pq}$ from $\bar{\theta}_{IA}$ or $\bar{c}_{I\Phi}$ are

$$\bar{D}_{rs} \mathrel{+}= \sum_{IA} 2w_I \cdot T^{IA}_{rs}\bar{\theta}_{IA} \tag{49}$$

$$\bar{D}_{rs} \mathrel{+}= \sum_{I\Phi\Phi'\sigma} 2w_I \cdot \bar{c}_{I\Phi}\langle\Phi|a^{\dagger}_{r\sigma}a_{s\sigma}|\Phi'\rangle c_{I\Phi'} = \sum_{I} 2w_I \cdot \tilde{\gamma}_{rs}[\bar{\mathbf{c}}_I, \mathbf{c}_I] \tag{50}$$

where we have used the operation $\tilde{\gamma}$ in Eq.7.

To summarize this section, using the operations Eq.2, Eq.3, Eq.7 and Eq.8 listed at the beginning, we develop a direct compatible coupled perturbed solver for SA-CASSCF in PCM, which doesn't require the storage of the additional Hessian components related to the PCM surface charges. As shown in the right column of Table II, this requires expanding the existing gas phase coupled perturbed solver with Eq.38 through Eq.50.

2. Effective density matrices and integral nuclear gradients

In the gas phase SA-CASSCF, once the Lagrange multipliers are solved, the nuclear gradients can be computed as

$$\frac{dE_\Theta}{d\xi} = \frac{\partial L^{(\mathrm{SA})}_\Theta}{\partial\xi} = \frac{d\epsilon^{(\mathrm{nuclei})}}{d\xi} + \sum_{pq}\gamma^{\Theta}_{pq}\frac{\partial h_{pq}}{\partial\xi} + \sum_{pqrs}\Gamma^{\Theta}_{pqrs}\frac{\partial(pq|rs)}{\partial\xi} - \sum_{pq}X^{\Theta}_{pq}\frac{\partial S_{pq}}{\partial\xi} \tag{51}$$

γ^{Θ}_{pq} and Γ^{Θ}_{pqrs} are the effective density matrices that incorporate the target state density matrices $\mathbf{P^{\Theta}}$ and $\mathbf{\Pi^{\Theta}}$ as well as the corresponding Lagrange multiplisers $\bar{\boldsymbol{\kappa}}^{\Theta}$ and $\bar{\boldsymbol{\theta}}^{\Theta}$. X^{Θ}_{pq} is the effective Lagrangian. Similarly, when PCM is incorporated, we have $\frac{dE^{(\mathrm{PCM})}_\Theta}{d\xi} = \frac{\partial L^{(\mathrm{SA\text{-}PCM})}_\Theta}{\partial\xi}$.

To best reuse the gas phase codes, we will separate $L_\Theta^{(\text{SA-PCM})}$ into $L_\Theta^{(\text{SA})}$ and $\Lambda_\Theta^{(\text{SA-PCM})}$, where the latter denotes terms that are unique to PCM. This leads to

$$\frac{dE_\Theta^{(\text{PCM})}}{d\xi} = \frac{\partial L_\Theta^{(\text{SA-PCM})}}{\partial \xi} = \frac{\partial L_\Theta^{(\text{SA})}}{\partial \xi} + \frac{\partial \Lambda_\Theta^{(\text{SA-PCM})}}{\partial \xi} \tag{52}$$

$$\Lambda_\Theta^{(\text{SA-PCM})} = \Delta_\Theta^{(\text{PCM})} + \sum_{pq} \bar{\kappa}_{pq}^\Theta \frac{\partial \Delta^{(\text{SA-PCM})}}{\partial \kappa_{pq}} + \sum_{RS} \bar{\theta}_{RS}^\Theta \frac{\partial \Delta^{(\text{SA-PCM})}}{\partial \theta_{RS}} + \sum_n \bar{q}_n^\Theta \frac{\partial \Delta^{(\text{SA-PCM})}}{\partial q_n} \tag{53}$$

where $\Delta_\Theta^{(\text{PCM})}$ and $\Delta^{(\text{SA-PCM})}$ are defined in Eq.26 and Eq.13 respectively.

To compute Eq.52, note that the first term $\frac{\partial L_\Theta^{(\text{SA})}}{\partial \xi}$ is identical with Eq.51, thus we only need to consider how to compute $\frac{\partial \Lambda_\Theta^{(\text{SA-PCM})}}{\partial \xi}$. In particular, in order to use the operations for computing PCM integral gradients as defined in Eq.4, Eq.5 and Eq.6, we will try to formulate it in the form of

$$\frac{\partial \Lambda_\Theta^{(\text{SA-PCM})}}{\partial \xi} = \beta^\xi \left[\mathbf{D}^{(\Theta,1)}, \mathbf{q}\right] + \beta^\xi \left[\mathbf{D}^{(\Theta,2)}, \bar{\mathbf{q}}^\Theta\right] + B^\xi \left[\mathbf{s}^{(\Theta,\text{B})}\right] + A^\xi \left[\mathbf{s}^{(\Theta,\text{A1})}, \mathbf{s}^{(\Theta,\text{A2})}\right] - \sum_{pq} \lambda_{pq}^\Theta \frac{\partial S_{pq}}{\partial \xi} \tag{54}$$

The additional Lagrangian λ_{pq} can be computed as

$$\lambda_{pq}^\Theta = \sum_\mu C_{p\mu} \frac{\partial \Delta_\Theta^{(\text{PCM})}}{\partial C_{q\mu}} + \sum_\mu C_{q\mu} \frac{\partial \Delta_\Theta^{(\text{PCM})}}{\partial C_{p\mu}} = 2\sum_r P_{rp}^\Theta \tilde{V}_{rq}[\mathbf{q}] + 2\sum_r P_{rq}^\Theta \tilde{V}_{rp}[\mathbf{q}] \tag{55}$$

To determine $\mathbf{D}^{(\Theta,1)}$, $\mathbf{D}^{(\Theta,2)}$, $\mathbf{s}^{(\Theta,\text{B})}$,$\mathbf{s}^{(\Theta,\text{A1})}$ and $\mathbf{s}^{(\Theta,\text{A2})}$, first note that the effective one-electron density matrix $\boldsymbol{\gamma}^\Theta$ is equal to $\mathbf{P}^\Theta + \left(\bar{\boldsymbol{\kappa}}^\Theta \cdot \frac{\partial}{\partial \boldsymbol{\kappa}} + \bar{\boldsymbol{\theta}}^\Theta \cdot \frac{\partial}{\partial \boldsymbol{\theta}}\right) \mathbf{P}^{(\text{SA})}$. Thus the first three terms in Eq.53 can be combined and written as

$$\Delta_\Theta^{(\text{PCM})} + \sum_{pq} \bar{\kappa}_{pq}^\Theta \frac{\partial \Delta^{(\text{SA-PCM})}}{\partial \kappa_{pq}} + \sum_{RS} \bar{\theta}_{RS}^\Theta \frac{\partial \Delta^{(\text{SA-PCM})}}{\partial \theta_{RS}} = \left(\sum_{pqn} \gamma_{pq}^\Theta \beta_{pq,n} q_n + \sum_{Nn} Z_N B_{N,n} q_n + \frac{1}{2}\sum_{mn} q_m A_{mn} q_n\right) \tag{56}$$

From Eq.13, the last term in Eq.53 can be written as

$$\sum_n \bar{q}_n^{\Theta} \frac{\partial \Delta^{(\text{SA-PCM})}}{\partial q_n} = \sum_{pqn} P_{pq}^{(\text{SA})} \beta_{pq,n} \bar{q}_n + \sum_{Nn} Z_N B_{N,n} \bar{q}_n + \sum_{mn} q_m A_{mn} \bar{q}_n \tag{57}$$

Therefore, by adding the above two equations together, we get

$$D_{pq}^{(\Theta,1)} = \gamma_{pq}^{\Theta}, D_{pq}^{(\Theta,2)} = P_{pq}^{(\text{SA})} \tag{58}$$

$$s_n^{(\text{B})} = q_n + \bar{q}_n, s_n^{(\text{A1})} = q_n, s_n^{(\text{A2})} = \frac{1}{2} q_n + \bar{q}_n \tag{59}$$

In summary, the analytical nuclear gradients of SA-CASSCF in PCM can be evaluated as

$$\begin{aligned} &\frac{dE_{\Theta}^{(\text{PCM})}}{d\xi} = \frac{d\epsilon^{(\text{nuclei})}}{d\xi} + \sum_{pq} \gamma_{pq}^{\Theta} \frac{\partial h_{pq}}{\partial \xi} + \sum_{pqrs} \Gamma_{pqrs}^{\Theta} \frac{\partial (pq|rs)}{\partial \xi} - \sum_{pq} \left(X_{pq}^{\Theta} + \lambda_{pq}^{\Theta} \right) \frac{\partial S_{pq}}{\partial \xi} \\ &+ \beta^{\xi} \left[\boldsymbol{\gamma}^{\Theta}, \mathbf{q} \right] + \beta^{\xi} \left[\mathbf{P}^{(\text{SA})}, \bar{\mathbf{q}} \right] + B^{\xi} \left[\mathbf{q} + \bar{\mathbf{q}} \right] + A^{\xi} \left[\mathbf{q}, \tfrac{1}{2} \mathbf{q} + \bar{\mathbf{q}} \right] \end{aligned} \tag{60}$$

where γ_{pq}^{Θ}, Γ_{pqrs}^{Θ} and X_{pq}^{Θ} are computed with the gas phase codes, and β^{ξ}, B^{ξ} and A^{ξ} are computed with the existing GPU kernels. The additional operations needed for adding PCM into SA-CASSCF analytical gradients are shown in the right column of Table II.

C. Non-adiabatic coupling

The non-adiabatic coupling vector between SA-CASSCF wavefunctions[61] is defined as

$$d_{\xi}^{\Theta\Pi} = \langle \Psi_{\Theta} | \frac{d}{d\xi} \Psi_{\Pi} \rangle = -\frac{1}{E_{\Theta} - E_{\Pi}} \frac{d\Omega_{\Theta\Pi}}{d\xi} + \delta_{\xi}^{\Theta\Pi} \tag{61}$$

$\Omega_{\Theta\Pi}$ in the first term can be expressed as

$$\Omega_{\Theta\Pi} = \sum_{pq} T_{pq}^{\Theta\Pi} h_{pq} + \sum_{pqrs} \Xi_{pqrs}^{\Theta\Pi} (pq|rs) \tag{62}$$

where $\mathbf{T}^{\Theta\Pi}$ and $\boldsymbol{\Xi}^{\Theta\Pi}$ are one-electron and two-electron transition density matrices between the two target states Θ and Π. As shown in previous works,[49,61] the calculations of its nuclear derivatives are highly similar to the calculations of energy nuclear gradients. The second term $\delta_{\xi}^{\Theta\Pi}$ is computed from derivatives of overlap integrals

$$\delta_{\xi}^{\Theta\Pi} = \frac{1}{2}\sum_{rs}\left(T_{rs}^{\Theta\Pi} - T_{sr}^{\Theta\Pi}\right)\cdot\left(\langle\phi_r|\frac{d}{d\xi}\phi_s\rangle - \langle\frac{d}{d\xi}\phi_r|\phi_s\rangle\right) \tag{63}$$

These discussions indicate that the calculations of NAC with PCM will reuse many of the equations derived in Section II B.

When PCM is included, $\Omega_{\Theta\Pi}$ is modified as

$$\Omega_{\Theta\Pi}^{(\mathrm{PCM})} = \Omega_{\Theta\Pi} + \Delta_{\Theta\Pi}^{(\mathrm{PCM})} \tag{64}$$

where

$$\Delta_{\Theta\Pi}^{(\mathrm{PCM})} = \sum_{pq,n} T_{pq}^{\Theta\Pi}\beta_{pq,n}q_n \tag{65}$$

The corresponding Lagrangian is then defined by replacing $E_{\Theta}^{(\mathrm{PCM})}$ in Eq.27 with $\Omega_{\Theta\Pi}^{(\mathrm{PCM})}$, i.e.

$$L_{\Theta\Pi}^{(\text{SA-PCM})} = \Omega_{\Theta\Pi}^{(\mathrm{PCM})} + \sum_{pq}\bar{\kappa}_{pq}^{\Theta\Pi}\frac{\partial E^{(\text{SA-PCM})}}{\partial\kappa_{pq}} + \sum_{RS}\bar{\theta}_{RS}^{\Theta\Pi}\frac{\partial E^{(\text{SA-PCM})}}{\partial\theta_{RS}} + \sum_{n}\bar{q}_{n}^{\Theta\Pi}\frac{\partial E^{(\text{SA-PCM})}}{\partial q_n} \tag{66}$$

Enforcing the conditions in Eq.28 will lead to the coupled perturbed equations, where the left hand side of the coupled perturbed equation is identical with Eq.29. For the right hand side, the orbital gradient $\mathbf{g}^{(\mathrm{O;PCM}),\Theta\Pi}$ is computed with the gas phase code by replacing h_{pq} with η_{pq}. The charge gradient is computed as

$$g_n^{(\mathrm{Q;PCM}),\Theta\Pi} = \frac{\partial\Delta_{\Theta\Pi}^{(\mathrm{PCM})}}{\partial q_n} = \tilde{U}_n[\mathbf{T}^{\Theta\Pi}] \tag{67}$$

Solving the coupled perturbed equation will give the Lagrange multipliers, which can then be used to construct the effective density matrices. Note that $\Delta_{\Theta\Pi}^{(\mathrm{PCM})}$ in Eq.65 only has the electronic part compared to $E_{\Theta}^{(\mathrm{PCM})}$ in Eq.26. Thus following the derivations in Section II B, the non-adiabatic couplings can be computed as

$$\begin{aligned} d_{\xi}^{\Theta\Pi} = \delta_{\xi}^{\Theta\Pi} - \tfrac{1}{E_{\Theta}^{(\mathrm{PCM})} - E_{\Theta}^{(\mathrm{PCM})}}\{&\sum_{pq}\gamma_{pq}^{\Theta\Pi}\tfrac{\partial h_{pq}}{\partial\xi} + \sum_{pqrs}\Gamma_{pqrs}^{\Theta\Pi}\tfrac{\partial(pq|rs)}{\partial\xi} - \sum_{pq}\left(X_{pq}^{\Theta\Pi} + \lambda_{pq}^{\Theta\Pi}\right)\tfrac{\partial S_{pq}}{\partial\xi} \\ &+\beta^{\xi}\left[\boldsymbol{\gamma}^{\Theta\Pi},\mathbf{q}\right] + \beta^{\xi}\left[\mathbf{P}^{(\mathrm{SA})},\bar{\mathbf{q}}\right] + B^{\xi}\left[\bar{\mathbf{q}}\right] + A^{\xi}\left[\mathbf{q},\bar{\mathbf{q}}\right]\} \end{aligned} \tag{68}$$

where

$$\lambda_{pq}^{\Theta\Pi} = 2\sum_r T_{rp}^{\Theta\Pi}\tilde{V}_{rq}[\mathbf{q}] + 2\sum_r T_{rq}^{\Theta\Pi}\tilde{V}_{rp}[\mathbf{q}] \tag{69}$$

Similar to gradient calculations, the effective transition density matrices $\gamma_{pq}^{\Theta\Pi}$, $\Gamma_{pqrs}^{\Theta\Pi}$ and the effective Lagrangian $X_{pq}^{\Theta\Pi}$ are computed using the gas phase codes.

The above algorithm for computing non-adiabatic couplings of SA-CASSCF in PCM is summarized in Table III. The algorithm reuses most of the steps from the gradient algorithm in Table II and the only differences are Eq.67 through 69.

D. Dynamic weights

As discussed in the introduction, using dynamic weight methods provides a way to automatically adjusted the weight based on the energy differences from the state of interests as[31]

$$w_I = \frac{f\left(E_I - E_{\text{Ref}}\right)}{\sum_J f\left(E_J - E_{\text{Ref}}\right)} \tag{70}$$

By choosing a bandwidth parameter Δ and a weight formula $g(x)$, we define $f(x) = g(|x|/\Delta)$. Two types of weight formulas have been proposed before. One formula is based on cubic spline function,[38] where $g_{\text{cubic}}(x) = 1 - 3x^2 + 2x^3$ for $x \in [0, 1]$, and $g_{\text{cubic}}(x) = 0$ for $x > 1$. Another formula is based on the secant hyperbolic function,[39] where $g_{\text{sech2}}(x) = \text{sech}^2(\beta x)$. We set $\beta = 1.75$, such that $g_{\text{sech2}}(0.5) \approx g_{\text{cubic}}(0.5) = 0.5$. Both $g_{\text{cubic}}(x)$ and $g_{\text{sech2}}(x)$ satisfy that $g(0) = 1$, $g'(0) = 0$. However, they behave differently at $x \geq 1$. At these values, $g_{\text{cubic}}(x)$ are strictly zero. In contrast, $g_{\text{sech2}}(x)$ still has non-negligible value at $x = 1$ and exhibits a long tail for $x > 1$ (see Figure S5 in the supporting information). Both formulas will be tested in this work.

To compute the gradients for DW-SA-CASSCF in the gas phase, one additional term needs to be added to the Lagrangian corresponding to the contraints of the weights[44]

$$L_\Theta^{(\text{DW-SA})} = L_\Theta^{(\text{SA})} + \sum_I \bar{w}_I^\Theta \cdot \tau_I \tag{71}$$

$$\tau_I(\mathbf{E}) = w_I - \frac{f\left(E_I - E_{\mathrm{Ref}}\right)}{\sum_J f\left(E_J - E_{\mathrm{Ref}}\right)} \tag{72}$$

The Lagrange multipliers are determined to satisfy the following three conditions simultaneously,

$$\frac{\partial L_{\Theta}^{(\mathrm{DW\text{-}SA})}}{\partial \kappa_{rs}} = 0, \frac{\partial L_{\Theta}^{(\mathrm{DW\text{-}SA})}}{\partial \theta_{RS}} = 0, \frac{\partial L_{\Theta}^{(\mathrm{DW\text{-}SA})}}{\partial w_I} = 0 \tag{73}$$

and this leads to the coupled perturbed equations for DW-SA-CASSCF

$$\begin{pmatrix} \mathbf{H}^{(\mathrm{OO})} & \mathbf{H}^{(\mathrm{OC})} & \mathbf{W}^{(\mathrm{OW})} \\ \mathbf{H}^{(\mathrm{CO})} & \mathbf{H}^{(\mathrm{CC})} & \mathbf{0} \\ \mathbf{H}^{(\mathrm{WO})} & \mathbf{0} & \mathbf{I} \end{pmatrix} \begin{pmatrix} \bar{\boldsymbol{\kappa}}^{\Theta} \\ \bar{\boldsymbol{\theta}}^{\Theta} \\ \bar{\mathbf{w}}^{\Theta} \end{pmatrix} = \begin{pmatrix} -\mathbf{g}^{(\mathrm{O}),\Theta} \\ \mathbf{0} \\ \mathbf{0} \end{pmatrix} \tag{74}$$

where $H_{I,pq}^{(\mathrm{WO})} = \frac{\partial^2 E^{(\mathrm{SA})}}{\partial w_I \partial \kappa_{pq}}$, $W_{pq,I}^{[(\mathrm{OW})} = \frac{\partial \tau_I}{\partial \kappa_{pq}}$. Note that the left hand side is no longer symmetric, but can still be solved iteratively using matrix-vector product.[44] Once the coupled perturbed equation is solved, the effective density matrices γ_{pq}^{Θ}, Γ_{pqrs}^{Θ}, and X_{pq}^{Θ} will be constructed to incorporate all the three multipliers $\bar{\boldsymbol{\kappa}}^{\Theta}$,$\bar{\boldsymbol{\theta}}^{\Theta}$and $\bar{\mathbf{w}}^{\Theta}$.

Similarly, when PCM is added to DW-SA-CASSCF, we can define the Lagrangian by adding the weight constraint Eq.72 to Eq.27:

$$L_{\Theta}^{(\mathrm{DW\text{-}SA\text{-}PCM})} = L_{\Theta}^{(\mathrm{SA\text{-}PCM})} + \sum_I \bar{w}_I^{\Theta} \cdot \tau_I \tag{75}$$

The four types of Lagrange multipliers are solved by satisfying the four conditions simultaneously

$$\frac{\partial L^{(\mathrm{DW\text{-}SA\text{-}PCM})}}{\partial \kappa_{pq}} = 0, \frac{\partial L^{(\mathrm{DW\text{-}SA\text{-}PCM})}}{\partial \theta_{RS}} = 0, \frac{\partial L^{(\mathrm{DW\text{-}SA\text{-}PCM})}}{\partial w_I} = 0, \frac{\partial L^{(\mathrm{DW\text{-}SA\text{-}PCM})}}{\partial q_n} = 0 \tag{76}$$

which leads to the following coupled perturbed equation

$$\begin{pmatrix} \mathbb{H}^{(\mathrm{OO})} & \mathbb{H}^{(\mathrm{OC})} & \mathbb{W}^{(\mathrm{OO})} & \mathbb{H}^{(\mathrm{OQ})} \\ \mathbb{H}^{(\mathrm{CO})} & \mathbb{H}^{(\mathrm{CC})} & \mathbf{0} & \mathbb{H}^{(\mathrm{CQ})} \\ \mathbb{H}^{(\mathrm{WO})} & \mathbf{0} & \mathbf{I} & \mathbb{H}^{(\mathrm{WQ})} \\ \mathbb{H}^{(\mathrm{QO})} & \mathbb{H}^{(\mathrm{QC})} & \mathbb{W}^{(\mathrm{QW})} & \mathbb{H}^{(\mathrm{QQ})} \end{pmatrix} \begin{pmatrix} \bar{\boldsymbol{\kappa}}^{\Theta} \\ \bar{\boldsymbol{\theta}}^{\Theta} \\ \bar{\mathbf{w}}^{\Theta} \\ \bar{\mathbf{q}}^{\Theta} \end{pmatrix} = \begin{pmatrix} -\mathbf{g}^{(\mathrm{O}),\Theta} \\ \mathbf{0} \\ \mathbf{0} \\ -\mathbf{g}^{(\mathrm{Q}),\Theta} \end{pmatrix} \tag{77}$$

Similar to the fixed-weight calculations, $\mathbb{W}^{(\mathrm{OO})}$and $\mathbb{H}^{(\mathrm{WO})}$can be computed with the gas phase codes by replacing h_{pq} with η_{pq}. For the new terms unique to PCM,

$$\mathbb{H}^{(\mathrm{WQ})}_{I,n} = \frac{\partial^2 E^{(\text{SA-PCM})}}{\partial w_I \partial q_n} = \frac{\partial E_I}{\partial q_n} = \sum_{pq} P^I_{pq} \beta_{pq,n} \tag{78}$$

$$\mathbb{W}^{(\mathrm{QW})}_{n,I} = \frac{\partial \tau_I}{\partial q_n} = \sum_K \frac{\partial E_K}{\partial q_n} \frac{\partial \tau_I}{\partial E_K} = \sum_{K,pq} P^K_{pq} \beta_{pq,n} \frac{\partial \tau_I}{\partial E_K} \tag{79}$$

To use the iterative solver, we need to compute the matrix-vector product . The additional contributions to $\boldsymbol{\sigma}^{(\mathrm{W})}$ from $\mathbb{H}^{(\mathrm{WQ})} \cdot \bar{\mathbf{q}}$ can be computed by using $\bar{\mathbf{V}}$ defined in Eq.36 as

$$\sigma^{(\mathrm{W})}_I \mathrel{+}= \sum_{pq} P^I_{pq} \cdot \bar{V}_{pq} \tag{80}$$

The additional contributions to $\boldsymbol{\sigma}^{(\mathrm{Q})}$ from $\mathbb{W}^{(\mathrm{QW})} \cdot \bar{\mathbf{w}}$ can be incorporated by updating $\bar{\mathbf{D}}$ in Eq.44 with

$$\bar{D}_{pq} \mathrel{+}= \sum_{KI} P^K_{pq} \cdot \frac{\partial \tau_I}{\partial E_K} \cdot \bar{w}_I \tag{81}$$

Once the four Lagrange multipliers are solved, the nuclear gradients can be computed in the same way as Eq.60. The above discussions can also be applied to the non-adiabatic couplings. In Table I, Table II and Table III, steps required when dynamic weights are enabled are highlighted with "[DW]".

III. RESULTS AND DISCUSSION

The method described in this work is implemented in the TERACHEM[62,63] quantum chemistry package (currently supporting atom-centered *spd* Gaussian basis sets). All calculations are performed on computing nodes with NVIDIA GeForce GTX 1080Ti GPUs and Intel Xeon E5-2637 CPUs. Geometry optimizations and minimal energy conical intersection (MECI) searches are calculated with geomeTRIC[64] software. Figures and tables in the supporting information (SI) will be referred to as SI-Figures and SI-Tables.

A. Test of accuracy and performance

We start with testing the accuracy of the new method by comparing the analytical nuclear gradients and non-adibatic couplings with numerical ones, and the results are presented in SI-Section 1. The calculations are performed with SA(2)-CASSCF(4,4)/PCM/6-31G* on molecule $C_3H_6N^+$ with both fixed equal weights as well as dynamic weights, and the numerical gradients are computed with 3-point central difference with displacement of 0.0005 Angstrom. For ground and excited state nuclear gradients, the root mean square in the differences between analytical and numerical results are all within 5e-7 Hartree/Bohr (see SI-Table S1 and S2 for equal weights, SI-Tables S4 and S5 for dynamic weights). For non-adiabatic couplings, the discrepancies between analytical and numerical results are larger, and the root mean square in the differences is 1.71e-5 Hartree/Bohr for equal weight (SI-Table S3) and 2.46e-5 Hartree/Bohr for dynamic weight (SI-Table S6). The larger differences in the non-adiabatic couplings are partially due to the fact that the first term in Eq.61 is divided by the energy gap (0.087 Hartree for equal weights and 0.070 Hartree for dynamic weights), thus increasing the absolute errors.

Regarding the performance, we focus on comparing the computational cost with and without PCM. The test system we use is a porphyrin-based photosensitizer (see the chemical structure of inset in Figure 1), where the four hydrogen atoms illustrated are subsituted with diethylaminopentyl side chains subsequently to increase the number of basis functions while fixing the active space sizes. The fully substituted porphyrin has been reported as a novel photosensitizer for photodynamic therapy.[65] Figure 1(a) compares the time for the first energy iteration between with and without PCM, and Figure 1(b) compares the total time needed to evaluate the corresponding analytical nuclear gradients. As shown in Figure 1, the additional time needed by including PCM effects is very small compared to the gas phase calculations ($< 15\%$). In SI-Figure S1, we plot the timings versus number of basis functions using logarithmic scale axes, and use a power law fit to estimate the scaling. For a fixed active space, one of the major advantages of the atomic orbital formulation of SA-CASSCF energies and gradients in the gas phase is its near-quadratic scaling of computational cost with respect to the number of orbitals. SI-Figure S1 shows that this near-quadratic scaling is preserved when including PCM using the method developed in this work.

In addition to the time per iteration shown in Figure 1(a), the total time needed for computing the energy also depends on the convergence speed. The algorithm described in Section II A decouples the optimizations of CI and MO coefficients in the same manner as the gas phase implementation, and is known to be sensitive to the quality of the initial guess.[66,67] In practical applications including geometry optimizations, MECI searches and ab initio molecular dynamics simulations, the initial guess is often taken from the converged wavefunction of a nearby geometry. Therefore, we think it's more informative to test the convergence speed in similar settings. In SI-Section 3.1, we show the distributions of number of iterations in energy calculations both with and without PCM. The data is gathered from the calculations of Figure 2, in which the geometry is scanned from the Franck-Condon point to the MECI. As shown in SI-Figure S3, the numbers of iterations to reach convergence are very similar between calculations with and without PCM. For completeness, we also compare the number of iterations needed to converge the coupled perturbed equation in the gradient calculations. As shown in SI-Section 3.2, for all the systems tested, it takes around 15-25 iterations to converge the coupled perturbed equations in calculations with and without PCM.

We have also carried out similar tests on several retinal protonated Schiff base models[68] with increasing active space sizes. The results are provided in SI-Section 2 and 3, and the additional cost from using PCM is less than 20% compared to the gas phase calculations. Overall, these tests demonstrate that including the PCM effects into SA-CASSCF only result in a small additional computational cost for both energy and gradient calculations.

B. Effects of solvent polarity and dynamic weight bandwith on potential energy curves

In this section, we test how tuning the dielectric constant of PCM can change the potential energy curves along photoreaction pathways. Recently, Hoche et.al[69] synthesized a new dipolar merocyanine dye (merocyanine 4-(dicyanomethylene)-2-tert-butyl-6-[3-(3-butyl-benzothiazol-2-ylidene)1-propenyl]-4H-pyran, abbrievated as "DCBT", see inset of Figure 2(a)), and measured its optical properties in different solvents with increasing polarity. The major experimental observations include: (1) Large positive solvatochromism: The absorp-

tion maximum red-shifts from 534 nm in methylcyclohexane (MCH, $\epsilon = 2.02$) to 576 nm in dimethyl sulfoxide (DMSO, epsilon=46.7), and the fluorescence maximum also red-shifts from 546 nm in MCH to 637 nm in DMSO. (2) Strong increase of fluorescence quantum yield upon increasing solvent polarity, i.e., from 1% in MCH to 67% in DMSO. To help explain the experimental observations, Hoche et al. carried out SA-CASSCF calculation in the gas phase and identified two photoreaction pathways leading to two different MECIs, corresponding to photoisomerization around two different double bonds. However, reactions in solvents were only studied approximately using a two diabatic state model for the solute and the Onsager solvation model for the solvents. Because the new method developed in this work allows us to study the photoreaction pathways in solvent using SA-CASSCF/PCM directly, we can now compare calculations in gas phase and different solvents on the same footing.

We start by investigating the potential energy curves using equally-weighted SA-CASSCF. The critical point structures, i.e. the Franck-Condon (FC) point and the two MECIs, have been optimized for each environment individually, including gas phase, toluene($\epsilon = 2.38$), dichloromethane (ϵ =8.93), and DMSO($\epsilon = 46.7$). As shown in Figure 2(b), the critical point geometries in different environment are almost identical. We then generate paths connecting the FC point and the two MECIs using Nebterpolator[70], which provides a smooth interpolation in the internal coordinates of the molecules. At the FC point, Figure 2(a) clearly shows that the energy gap decreases with increasing polarity of the solvent, which is qualitatively consistent with the experimental observation. Compared to the FC point, the relative energies of the MECIs with respect to the ground state minimum are much less sensitive to the polarity of the solvent. Along the interpolated pathways, the energy profiles are barrierless for both gas phase and toluene. In contrast, small barriers appear for both dichloromethane and DMSO. Towards MECI-1, the highest point on the S1 surface is higher than the FC point by 0.19kcal/mol and 0.73 kcal/mol for dichlormethane and DMSO respectively. Towards MECI-2, the highest point on the S1 surface is higher than the FC point by 0.04kcal/mol and 0.96 kcal/mol for the two solvents. The observation that barriers appear and gradually increase with polarity of the solvents is qualitatively consistent with the experimental results of increasing fluorescent yield.

To help understand the experimental observations, Hoche et.al also devised a simple two diabatic state models,[69] and suggested that the changes of the dipole moments of the

molecules along the photoreaction pathways can help explain the effects of the solvent polarity. In SI-Figure S4, we show the dipole moments obtained from SA-CASSCF/PCM calculations. The figure clearly shows that the dipole moments of ground and excited states differ the most at the FC region. Thus, when increasing the polarity of the solvents, the excited state around FC will experience more stabilization effects than the ground state, leading to the solvatochromism phenomena. The difference in the dipole moment between ground and excited states gradually becomes smaller as the geometry approaches either of the MECIs. As a result, the potential energy curves around MECIs exhibit minimal changes when increasing the solvent polarity. Despite the qualitative agreement with experiments, the energy gap at the Frank-Condon point is larger than the experimental absorption by about 2 eV. One contributing factor is that PCM in equilibrium with the state averaged density underestimates that solvation effects of the excited state. Another important factor is that SA-CASSCF lacks dynamic correlation, and the spectrum obtained from SA-CASSCF is known to be systematically blue shifted compared to experiments.[71] A more accurate theoretical estimates of the absorption energy and barrier heights would require incorporating dynamic correlations (e.g. using multi-reference perturbation theory on top of SA-CASSCF) and performing transition state optimizations. These are beyond the scope of this work, and will be studied in the future.

The usage of dynamic weights is expected to improve the descriptions of solvation effects for the state of interest. Since we are primarily interested in the excited state properties of the molecule, we choose S1 as the reference state to compute the weights in Eq.70. The potential energy curves obtained with different bandwidths using the cubic spline formula are shown in Figure 3. From the solid lines in Figure 3(a), it is observed that using dynamic weights lowers the S1 energies around the FC point as expected, and provides the same results as equally weighted SA-CASSCF at MECIs. The weights along the pathways are shown in Figure 3(b), where the weights between S0 and S1 differ the most at FC and both gradually approach 0.5 at MECIs. In addition, Figure 3(a) shows that the shapes of the energy curves of S1 using different bandwidths are very close to each other, which is also true when the secant weight fomula is used (see SI-Figure S6). This suggests that the energies of the reference state are not very sensitive to the bandwidth parameter, which is desirable. We suggest choosing a bandwidth parameter slightly larger than the FC energy

gap calculated with equally weighted SA-CASSCF.

For the purpose of performing non-adiabatic molecular dynamics simulations (such as ab initio multiple spawning[72,73] and the surface hopping method[74,75]), the propagation of the trajectory at a particular time step is primarily determined by the state that the trajectory is on, which should naturally be chosen as the reference state. Although the other non-reference states do not apply forces to the trajectory directly, the probability of triggering non-adiabatic transition events is determined by the norm of the non-adiabatic couplings, which is roughly inversely proportional to the size of the energy gap. From the dashed lines in Figure 3(a), the energy gaps close to the MECIs are largely independent of the bandwidth. Although we don't expect the solvation energies of the non-reference states to be quantitatively accurate near the FC region, it's still concerning that the S0 energy curve becomes notably distorted around midpoints of both pathways when using the smallest bandwidth $\Delta = 2.4$ eV. By comparing with Figure 3(b), the distortion appears when the weights of S0 change from strictly zero to nonzero values. This observation may point to a drawback of using the cubic spline weight formula with overly small bandwidth values. By examining the wavefunctions (see SI-Figure S7 and S8), we found that the CI coefficients actually change smoothly around the region where the distortions occur. We think this suggests that the distortions in this specific case are not caused by root-flipping, although the precise source of the distortions is still unclear. Instead, when the secant weight formula is used, such distortions are no longer observed at the same bandwidth parameter (see SI-Figure S6).

The above discussion shows that dynamically weighted SA-CASSCF with PCM is appropriate for performing non-adiabatic molecular dynamics simulations. However, when computing properties along the non-adiabatic trajectories, one should be cautious if the property requires both the ground and excited states to be quantitatively accurate, such as time-dependent fluorescence. In these applications, it's necessary to recompute the ground state energies at each geometry along the trajectory by selecting S0 as the reference state, and piece the two results together to get the time-dependent signals.

C. Effects of solvent models on MECI geometries and topologies

As discussed in the introduction section, PCM primarily captures the electrostatic interactions between the solute and solvent, but is not able to capture other types of interactions such as hydrogen bonding. In this section, we will investigate how the solvent models affect the MECI geometries and topologies. This is important for simulating excited state dynamics in solvent, because conical intersections are critical for non-adiabatic transitions, and its topology can affect the excited state dynamics.[76]

For the green fluorescent protein[77] chromophore, theoretical studies have found that the topology around its MECI can be qualitatively different depending on its environment. The MECI is sloped (i.e. MECI is not a S1 local minimum) in the gas phase, but becomes peaked (i.e. MECI is at S1 local minimum) in water. This has been observed by solvating the chromophore with explicit solvents, both by using fixed-charge forcefield model[78] as well as by treating the water molecules (about 50 molecules) quantum mechanically.[49] Here we would like to understand if PCM is sufficient to reproduce the peaked topology. This will help reveal whether the changes in the topology is primarily due to electrostatic interactions or if other types of interactions are playing major roles.

We carried out four separate MECI optimizations for the green fluorescent protein chromophores (4´-hydroxybenzylidene-2,3-dimethylimidazolinone, p-HBDI) in four different environments (see Figure 4): gas phase, PCM ($\epsilon = 78.4$, corresponding to water) with no explcit solvent, in gas phase with 7 explicit quantum water molecules that form hydrogen bonds with the negatively charged oxygen atom, and finally in PCM with the 7 explicit quantum water molecules. Figure 4(a) compares the four optimized MECI structures. We observed that the MECI optimized in the gas phase is notably different from the other three MECIs that include some solvation effects. The illustrated dihedral angle is 53 degrees in the gas phase, 11 degrees with PCM, and nearly zero when including explicit water molecules (for both with and without PCM). This shows that solvation effects can change the conical intersection geometries in a non-trivial way, making it important to perform MECI searches in the presence of solvent.

In Figure 4(b) as well as SI-Figure S9, we present 3D plots showing the topology of PES around the MECI in the four different environment. All the four plots clearly show that the

surfaces are degenerate at the MECI, and the degeneracy is lifted in the $g-h$ branching plane, where g represents the normalized gradient difference vector, and h represents the normalized non-diabatic coupling vector. In order to compare the four surfaces directly, in Figure 4(c) and (d) we plotted 1D energy curves along the line of $g = 0$ and $h = 0$ respectively. We observed that along the line of $g = 0$ (Figure 4(d)), there are notable differences between gas phase and in solvent, but the differences between the three solvent models are small. In contrast, the different solvent models used show more significant differences along the line of $h = 0$ (Figure 4(c)). The MECI in the gas phase are clearly sloped, consistent with previous studies. The MECI in PCM is still sloped, but becomes peaked if hydrogen bonding is included. This suggests that the hydrogen bonds between the solvent and the chromophore play a bigger role for altering the MECI topology from sloped to peaked. However, this doesn't mean that the electrostatic interaction is not important and PCM is unnecessary. When comparing gas-phase calculations with 7 explicit waters (magenta) versus including 7 explicit waters with PCM (red), it is observed that one of the diabatic surface (upper left to lower right) is almost unchanged by PCM but the other diabatic surface is notably affected (lower left to upper right). As shown in SI-Figure S10, the latter diabatic surface has a larger dipole moment than the former (larger by around 15 debye), thus is more susceptible to the electrostatic effects of the solvent. Overall, these results show that both hydrogen bonding and PCM are important for correctly describing the topology of the MECI.

The above discussions show that solvents can have notable effects on both the conical intersection structures as well as the topology surrounding it. Compared with solvating the solute with a large number of explicit quantum solvent molecules, using PCM plus a few quantum solvent molecules that form hydrogen bonding with the solute provides a much more efficient alternative, in terms of reducing both the number of explicit atoms/basis functions and also the conformational sampling needed. In addition, using PCM to describe the solvent outside the envelope of explicit solvent mitigates the problem of dangling hydrogen bonds.

IV. CONCLUSIONS

In conclusion, we developed state-averaged CASSCF energies and gradients in PCM for both fixed and dynamic weights. This method is suitable for studying the solvation effects

on photochemistry where the polarity of the solvents plays a major role. The novel developments of analytical nuclear gradients and non-adiabatic couplings enable searching for conical intersections in solvents directly, and provide the required ingredients for carrying out solvated excited state non-diabatic molecular dynamics simulations in the future. By formulating the new method in terms of existing GPU kernels, including PCM only results in small additional computational cost, as demonstrated by performance tests. Studies on model chromophores show that solvents can have non-negligible effects over the photochemical processes, by tuning the barrier height along the photoreaction pathway as well as by changing the geometries and topologies around the conical intersections.

The SA-CASSCF used in this work only captures static correlation but lacks dynamic correlation, thus cannot provide quantatively accurate descriptions for potential energy surfaces. One rigorous way to include dynamic correlation is to apply perturbation theory on top of SA-CASSCF references, leading to the multi-state complete active space second order perturbation theory (MS-CASPT2).[79,80] In particular, a dynamic weight scheme for MS-CASPT2 has also been developed lately.[81,82] The development of the energies, analytical nuclear gradients and non-adiabatic couplings for MS-CASPT2 in PCM will allow more accurate predictions for photochemical processes in solvents. Furthermore, such methods will also be useful for benchmarking other approximate ways for including dynamic correlation, such as α-CASSCF[83] where the empirical parameter α is parametrized by fitting to MS-CASPT2 potential energy curves.

The PCM with fixed dielectric constant used in this work makes significant approximations by design, including the inability to describe the separation in time scales of fast (electronic) and slow (nuclear) polarization during excited state dynamics. We expect most of the theoretical framework developed in this work can be applied to other classical polarizable models that support separations of fast and slow polarization response. A few examples include polarizable force field models[22,23] commonly used for solvents and protein environments, and the discrete interaction model[84,85] often used for metal environments. Recently there has been progress made on carrying out excited state Bohn Oppenheimer molecular dynamic simulations by combining AMOEBA polarizable forcefield and TDDFT.[86] Along similar lines, we plan to generalize the ideas developed in this work to multi-reference methods in polarizable models with atomistic details, which will enable first-principles excited

state nondiabatic molecular dynamics simulations for studying photochemistry in complex chemical environments.

SUPPLEMENTARY MATERIAL

See supplemental material for additional test results for accuracy and performance, along with input and output files for calculations described in this work.

AUTHOR DECLARATION

The author has no conflicts to disclose.

DATA AVAILABILITY

Most of the data that supports the findings of this study are available within the article and its supplementary material except large-sized files. The latter are available from the corresponding author upon reasonable request.

ACKNOWLEDGEMENTS

This work was supported by the startup funds of the UC Davis Department of Chemistry. I would like to thank Dr. Lee-Ping Wang for helpful discussions.

TABLE I. Algorithm for energy calculations of SA-CASSCF with PCM. The left column shows the algorithm adapted from gas phase calculations. The algorithm supports both fixed weights and dynamic weights, where "[DW]" indicates steps required when dynamic weights are enabled. The right column shows new operations needed for including PCM.

(DW)-SA-CASSCF	**PCM**
Initialization	
Obtain guess MO coefficients $C_{p\mu}$	
[**DW**]: Initialize weights $w_I = 1/n_{\text{states}}$	
	Obtain guess PCM surface charges $\mathbf{q}$
Optimization	
loop	
Form required integrals including h_{pq}	
	Update one electron integrals: h_{pq} += $\tilde{V}_{pq}[\mathbf{q}]$ ▷Eq(16)
Solve CI coefficients and energies: $\hat{H}\Psi_I = E_I\Psi_I$	
[**DW**]: Update dynamic weights: $w_I = \frac{f(E_I - E_{\text{ref}})}{\sum_K f(E_K - E_{\text{ref}})}$	
Compute state-averaged density matrix $\mathbf{P}^{(\text{SA})}$	
Compute orbital gradients: $\mathbf{g}^{(\text{O})}$	
Get max residual: $g^{\max} = \|\|\mathbf{g}^{(\text{O})}\|\|_\infty$	
	Compute surface charge gradients: $\mathbf{g}^{(\text{Q})}$ ▷Eq(17)
	Update max residual: $g^{\max} = \max\left(g^{\max}, \|\|\mathbf{g}^{(\text{Q})}\|\|_\infty\right)$
if $g^{\max} <$ threshold **then return**	
Update MO coefficients using Newton-Raphson	
	Update surface charges from $\mathbf{g}^{(\text{Q})}$ ▷Eq(19)
end loop	

TABLE II. Algorithm for analytical nuclear gradient calculations of SA-CASSCF with PCM. The algorithm is presented in the same way as Table I.

(DW)-SA-CASSCF	**PCM**	
Initialization		
1 Obtain converged MO, CI coefficients and state energies		
	2 Obtain converged PCM surface charges $\mathbf{q}$	
3 Construct required integrals including h_{pq}		
	4 Update one electron integrals: h_{pq} +=$\tilde{V}_{pq}[\mathbf{q}]$	▷Eq(16)
5 Partially build Hessian: $\mathbb{H}^{(\mathrm{OO})}$,$\mathbb{H}^{(\mathrm{CO})}$, $\mathbb{H}^{(\mathrm{OC})}$and $\mathbb{H}^{(\mathrm{CC})}$		
6 [**DW**]: Partially build Hessian: $\mathbb{H}^{(\mathrm{WO})}$and $\mathbb{W}^{(\mathrm{OW})}$		
Coupled-perturbed equation		
7 Compute state orbital gradient: $\mathbf{g}^{(\mathrm{O}),\Theta}$		
	8 Compute state charge gradient: $\mathbf{g}^{(\mathrm{Q}),\Theta}$	▷Eq(30)
9 Initialize multipliers $\bar{\boldsymbol{\kappa}}^{\Theta}$ and $\bar{\boldsymbol{\theta}}^{\Theta}$		
10 [**DW**]: Initialize multipliers $\bar{\mathbf{w}}^{\Theta}$		
	11 Initialize multipliers $\bar{\mathbf{q}}^{\Theta}$	
12 **while** remainder > threshold **do**		
13 Build Hessian-trial vector product: $\boldsymbol{\sigma}^{(\mathrm{O})} = \mathbb{H}^{(\mathrm{OO})} \cdot \bar{\boldsymbol{\kappa}}^{\Theta} + \mathbb{H}^{(\mathrm{OC})} \cdot \bar{\boldsymbol{\theta}}^{\Theta}$ $\boldsymbol{\sigma}^{(\mathrm{C})} = \mathbb{H}^{(\mathrm{CO})} \cdot \bar{\boldsymbol{\kappa}}^{\Theta} + \mathbb{H}^{(\mathrm{CC})} \cdot \bar{\boldsymbol{\theta}}^{\Theta}$		
14 [**DW**]: Update Hessian-trial vector product: $\boldsymbol{\sigma}^{(\mathrm{O})}$ += $\mathbb{W}^{(\mathrm{OW})} \cdot \bar{\mathbf{w}}^{\Theta}$ $\boldsymbol{\sigma}^{(\mathrm{W})} = \mathbb{H}^{(\mathrm{WO})} \cdot \bar{\boldsymbol{\kappa}}^{\Theta} + \mathbb{I} \cdot \bar{\mathbf{w}}^{\Theta}$		
	15 Compute $\bar{V}_{pq} = \tilde{V}_{pq}[\bar{\mathbf{q}}]$	▷Eq(36)
	16 Update $\boldsymbol{\sigma}$ using $\bar{V}_{pq}$	
	Update $\boldsymbol{\sigma}^{(\mathrm{O})}$ with $\bar{V}_{pq}$	▷Eqs(38),(39),(40)
	Update $\boldsymbol{\sigma}^{(\mathrm{C})}$ with $\bar{V}_{pq}$	▷Eqs(41),(42),(43)
	[**DW**]: Update $\boldsymbol{\sigma}^{(\mathrm{W})}$ with $\bar{V}_{pq}$	▷Eq(80)
	17 Allocate and compute $\bar{D}_{pq}$	
	Update $\bar{D}_{pq}$ with $\bar{\boldsymbol{\kappa}}^{\Theta}$	▷Eqs(45),(46),(47)
	Update $\bar{D}_{pq}$ with $\bar{\boldsymbol{\theta}}^{\Theta}$	▷Eqs(48),(49),(50)
	[**DW**]: Update $\bar{D}_{pq}$ with $\bar{\mathbf{w}}^{\Theta}$	▷Eq(81)
	18 Compute $\boldsymbol{\sigma}^{(\mathrm{Q})}$ from $\bar{D}_{pq}$	▷Eq(44)
19 Update multipliers using $\boldsymbol{\sigma}$		
20 Update remainder		
21 **end while**		
Build effective density matrices		
22 Build γ^{Θ}_{pq}, Γ^{Θ}_{pqrs}, X^{Θ}_{pq} from $\bar{\boldsymbol{\kappa}}^{\Theta}$ and $\bar{\boldsymbol{\theta}}^{\Theta}$		
23 [**DW**]: Update γ^{Θ}_{pq} and Γ^{Θ}_{pqrs} from $\bar{\mathbf{w}}^{\Theta}$		
	24 Compute λ^{Θ}_{pq} and add to X^{Θ}_{pq}	▷Eq(55)
Compute integral nuclear gradients		
25 Add one-electron integral gradients using $\boldsymbol{\gamma}^{\Theta}$		
26 Add two-electron integral gradients using $\boldsymbol{\Gamma}^{\Theta}$		
27 Add overlap integral gradients using $\mathbf{X}^{\Theta}$		
28 Add nuclear repulsion energy gradients		
	29 Add PCM gradients with $\mathbf{q}$,$\bar{\mathbf{q}}$, $\boldsymbol{\gamma}^{\Theta}$ and $\mathbf{P}^{(\mathrm{SA})}$	▷Eq(60)

TABLE III. Algorithm for non-adiabatic coupling calculations of SA-CASSCF with PCM. The algorithm is presented in the same way as Table I.

(DW)-SA-CASSCF	**PCM**
Initialization	
1 Perform Steps 1 through 6 in Table II	
Coupled-peturbed equation	
2 Compute transition orbital gradient $\mathbf{g}^{(\mathrm{O}),\Theta\Pi}$	3 Compute transition charge gradient $\mathbf{g}^{(\mathrm{Q}),\Theta\Pi}$ ▷Eq(67)
4 Perform Steps 9 through 21 in Table II	
Build effective density matrices	
5 Build $\gamma_{pq}^{\Theta\Pi}$, $\Gamma_{pqrs}^{\Theta\Pi}$, $X_{pq}^{\Theta\Pi}$ from $\bar{\boldsymbol{\kappa}}^{\Theta\Pi}$ and $\bar{\boldsymbol{\theta}}^{\Theta\Pi}$	
6 [**DW**]: Update $\gamma_{pq}^{\Theta\Pi}$ and $\Gamma_{pqrs}^{\Theta\Pi}$ from $\bar{\mathbf{w}}^{\Theta\Pi}$	7 Compute $\lambda_{pq}^{\Theta\Pi}$ and add to $X_{pq}^{\Theta\Pi}$ ▷Eq(69)
Compute integral nuclear gradients	
8 Allocate G_ξ	
9 Add one-electron integral gradients to G_ξ using $\boldsymbol{\gamma}^{\Theta\Pi}$	
10 Add two-electron integral gradients to G_ξ using $\boldsymbol{\Gamma}^{\Theta\Pi}$	
11 Add overlap integral gradients to G_ξ using $\mathbf{X}^{\Theta\Pi}$	12 Add PCM gradients to G_ξ with $\mathbf{q}$,$\bar{\mathbf{q}}$,$\boldsymbol{\gamma}^{\Theta\Pi}$ and $\mathbf{P}^{(\mathrm{SA})}$ ▷Eq(68)
13 Compute NAC: $d_\xi^{\Theta\Pi} = -\frac{1}{E_\Theta - E_\Pi} G_\xi + \delta_\xi^{\Theta\Pi}$	

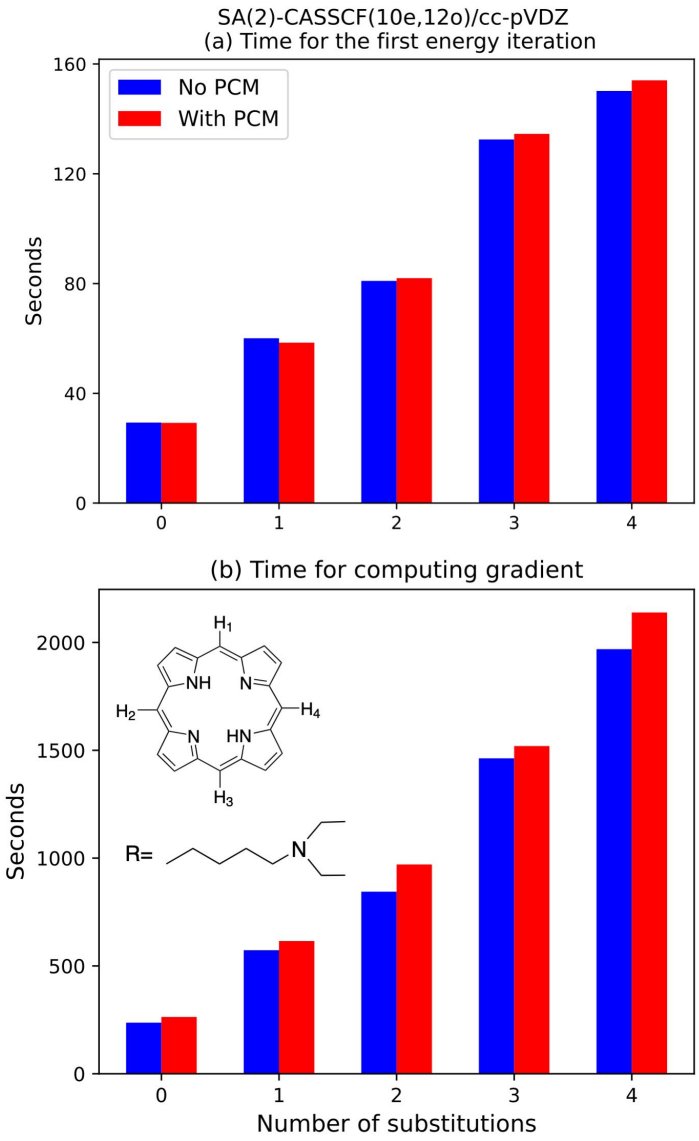

FIG. 1. Timing for SA-CASSCF calculations in PCM. The inset chemical structures represent the test systems, where the four hydrogen atoms H_1, H_2, H_3, and H_4 of the porphyrin are substituted with the side group R one at a time. Equal weights are used in state-averaging. (a) shows the timing for the first iteration in energy calculations, and (b) shows the total timing for computing the ground state nuclear gradients.

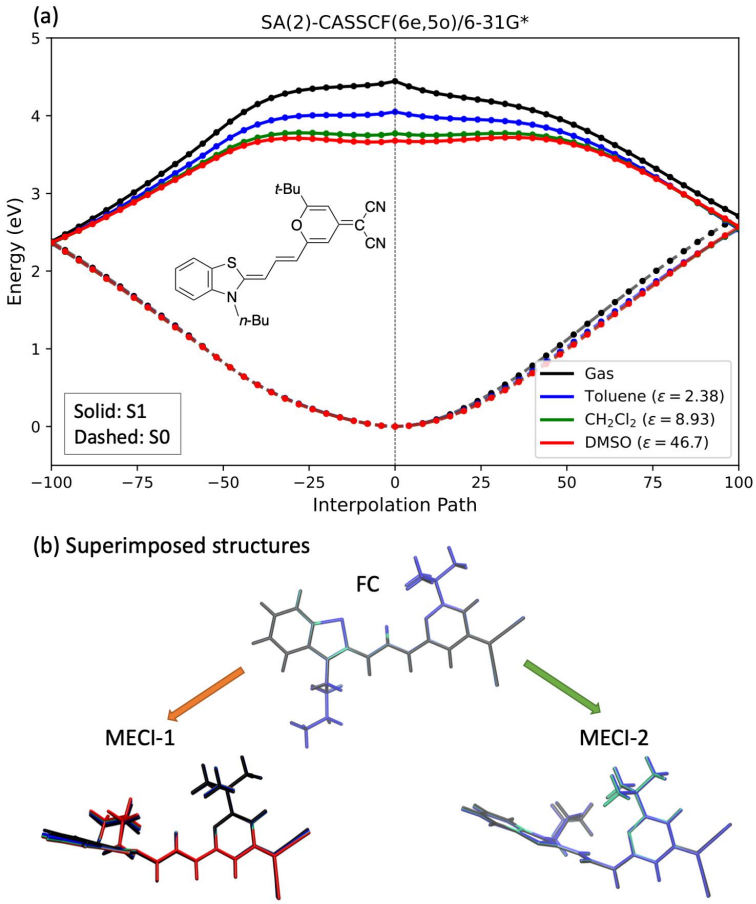

FIG. 2. Effects of polarity of the solvents over the potential energy curves of DCBT molecule (see the inset chemical structure). (a) shows the potential energy curves along the interpolation paths in different solvents from the Franck-Condon point (FC, $x = 0$) to the two minimal energy conical intersections (MECI-1 at $x = -100$ and MECI-2 at $x = 100$). The FC and MECIs are optimized for each solvent, thus the interpolation is performed for each solvent separately. (b) shows the superimposed optimized structures from different solvents, where the colors of the structure are consistent with the line colors in (a).

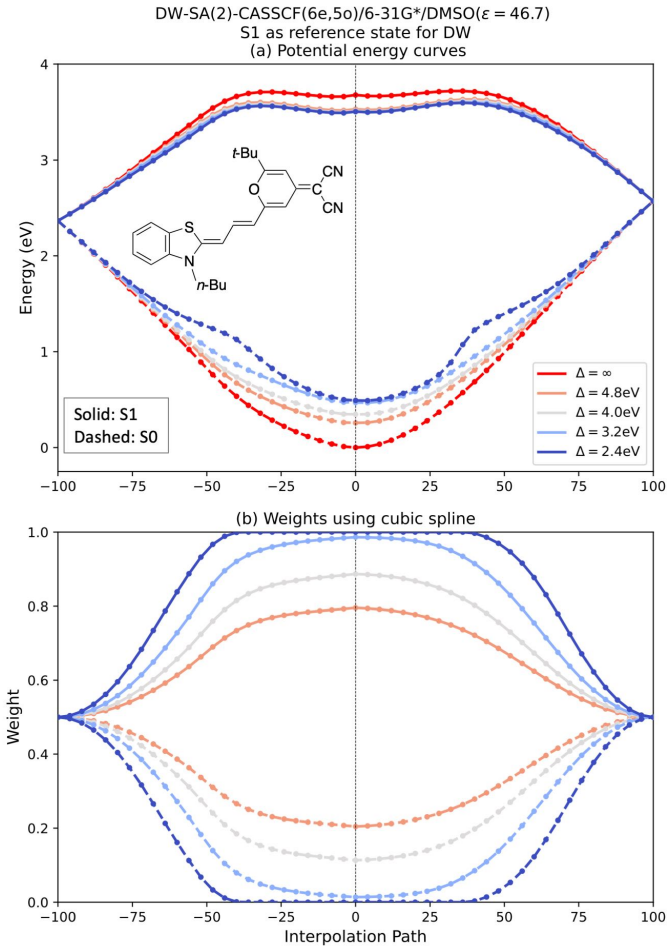

FIG. 3. Effects of bandwidth in dynamic weights over the potential energy curves of DCBT molecule. The dynamic weights are computed with the cubic spline functions. The excited state S1 is chosen as the reference state. The interpolation path in DMSO from Figure 2 is used for all calculations. (a) shows the potential energy curves generated using different bandwidth, and (b) shows the corresponding weights for ground and excited states.

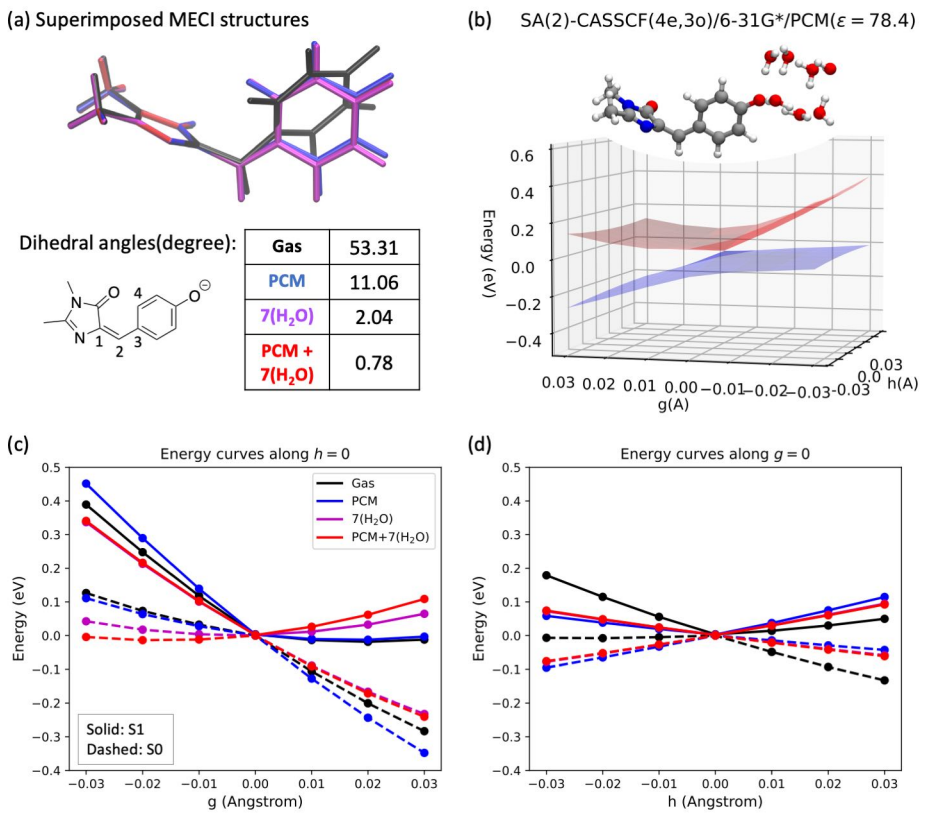

FIG. 4. Effects of solvent models over conical intersection geometries and topology of HBDI chromophore. Four different environments are tested: in gas phase (black), adding PCM (blue), adding 7 explicit water molecules that form hydrogen bonds with the chromophore (magenta), and adding both PCM and the 7 explicit water molecules. (a) shows the superimposed MECI optimized structures, where the four calculations differ in the denoted dihedral angle with values provided in the table. (b) shows the potential energy surfaces around the MECI when adding both PCM and explicit waters. Similar figures for the other three calculations can be found in supporting information. (c) and (d) compare the topology around the MECI in the four environments by plotting the 1D potential energy curves along $h = 0$ and $g = 0$ respectively. g represents displacement along the normalized gradient difference vector, and h represents displacement along the normalized nonadiabatic coupling vector.

REFERENCES

[1]T. Kumpulainen, B. Lang, A. Rosspeintner, and E. Vauthey, Chemical Reviews **117**, 10826 (2017).

[2]G. R. Fleming, S. H. Courtney, and M. W. Balk, Journal of Statistical Physics **42**, 83 (1986).

[3]J. Saltiel and J. T. D'Agostino, Journal of the American Chemical Society **94**, 6445 (1972).

[4]M. Quick, A. L. Dobryakov, M. Gerecke, C. Richter, F. Berndt, I. N. Ioffe, A. A. Granovsky, R. Mahrwald, N. P. Ernsting, and S. A. Kovalenko, The Journal of Physical Chemistry B **118**, 8756 (2014).

[5]A. Kahan, A. Wand, S. Ruhman, S. Zilberg, and Y. Haas, The Journal of Physical Chemistry A **115**, 10854 (2011).

[6]X. F. Xu, A. Kahan, S. Zilberg, and Y. Haas, The Journal of Physical Chemistry. A **113**, 9779 (2009).

[7]A. DeFusco, N. Minezawa, L. V. Slipchenko, F. Zahariev, and M. S. Gordon, The Journal of Physical Chemistry Letters **2**, 2184 (2011).

[8]T. J. Zuehlsdorff, P. D. Haynes, F. Hanke, M. C. Payne, and N. D. M. Hine, Journal of Chemical Theory and Computation **12**, 1853 (2016).

[9]W. Domcke and D. R. Yarkony, Annual Review of Physical Chemistry **63**, 325 (2012).

[10]B. G. Levine, J. D. Coe, and T. J. Martínez, The Journal of Physical Chemistry B **112**, 405 (2008).

[11]B. F. E. Curchod and T. J. Martínez, Chemical Reviews **118**, 3305 (2018).

[12]B. Mennucci, Theoretical Chemistry Accounts **116**, 31 (2006).

[13]M. Cossi and V. Barone, The Journal of Physical Chemistry A **104**, 10614 (2000).

[14]M. Cossi and V. Barone, The Journal of Chemical Physics **112**, 2427 (2000).

[15]B. Mennucci, WIREs Computational Molecular Science **2**, 386 (2012).

[16]A. Klamt and G. Schüürmann, Journal of the Chemical Society, Perkin Transactions 2 **0**, 799 (1993).

[17]J. M. Herbert, WIREs Computational Molecular Science **11**, e1519 (2021).

[18]F. Ding, D. B. Lingerfelt, B. Mennucci, and X. Li, Journal of Chemical Physics **142**, 034120 (2015).

[19]H. W. Horn, W. C. Swope, J. W. Pitera, J. D. Madura, T. J. Dick, G. L. Hura, and T. Head-Gordon, The Journal of Chemical Physics **120**, 9665 (2004).

[20]W. L. Jorgensen, J. Chandrasekhar, J. D. Madura, R. W. Impey, and M. L. Klein, The Journal of Chemical Physics **79**, 926 (1983).

[21]L.-P. Wang, T. J. Martinez, and V. S. Pande, The Journal of Physical Chemistry Letters **5**, 1885 (2014).

[22]M. L. Laury, L.-P. Wang, V. S. Pande, T. Head-Gordon, and J. W. Ponder, The Journal of Physical Chemistry B **119**, 9423 (2015).

[23]P. Ren and J. W. Ponder, The Journal of Physical Chemistry B **107**, 5933 (2003).

[24]S. S. Xantheas, C. J. Burnham, and R. J. Harrison, The Journal of Chemical Physics **116**, 1493 (2002).

[25]G. Lamoureux, E. Harder, I. V. Vorobyov, B. Roux, and A. D. MacKerell, Chemical Physics Letters **418**, 245 (2006).

[26]M. Bondanza, M. Nottoli, L. Cupellini, F. Lipparini, and B. Mennucci, Physical Chemistry Chemical Physics **22**, 14433 (2020).

[27]M. Casida and M. Huix-Rotllant, Annual Review of Physical Chemistry **63**, 287 (2012).

[28]M. E. Casida, in *Recent Advances in Density Functional Methods*, Recent Advances in Computational Chemistry, Vol. Volume 1 (WORLD SCIENTIFIC, 1995) pp. 155–192.

[29]B. G. Levine, C. Ko, J. Quenneville, and T. J. MartÍnez, Molecular Physics **104**, 1039 (2006).

[30]H. Lischka, D. Nachtigallová, A. J. A. Aquino, P. G. Szalay, F. Plasser, F. B. C. Machado, and M. Barbatti, Chemical Reviews **118**, 7293 (2018).

[31]M. A. Hagras and W. J. Glover, Journal of Chemical Theory and Computation **14**, 2137 (2018).

[32]M. A. Thompson, The Journal of Physical Chemistry **100**, 14492 (1996).

[33]R. Cammi, L. Frediani, B. Mennucci, and K. Ruud, The Journal of Chemical Physics **119**, 5818 (2003).

[34]C. Curutchet, A. Muñoz-Losa, S. Monti, J. Kongsted, G. D. Scholes, and B. Mennucci, Journal of Chemical Theory and Computation **5**, 1838 (2009).

[35]R. Improta, V. Barone, G. Scalmani, and M. J. Frisch, The Journal of Chemical Physics **125**, 054103 (2006).

[36]R. Cammi, L. Frediani, B. Mennucci, J. Tomasi, K. Ruud, and K. V. Mikkelsen, The Journal of Chemical Physics **117**, 13 (2002).

[37]Q. Li, B. Mennucci, M. A. Robb, L. Blancafort, and C. Curutchet, Journal of Chemical Theory and Computation **11**, 1674 (2015).

[38]W. J. Glover, The Journal of Chemical Physics **141**, 171102 (2014).

[39]M. P. Deskevich, D. J. Nesbitt, and H.-J. Werner, The Journal of Chemical Physics **120**, 7281 (2004).

[40]R. Dawes, A. W. Jasper, C. Tao, C. Richmond, C. Mukarakate, S. H. Kable, and S. A. Reid, The Journal of Physical Chemistry Letters **1**, 641 (2010).

[41]B. O. Roos, P. R. Taylor, and P. E. M. Sigbahn, Chemical Physics **48**, 157 (1980).

[42]B. O. Roos, International Journal of Quantum Chemistry **18**, 175 (1980).

[43]M. W. Schmidt and M. S. Gordon, Annual Review of Physical Chemistry **49**, 233 (1998).

[44]W. J. Glover, A. S. P. Paz, W. Thongyod, and C. Punwong, The Journal of Chemical Physics **151**, 201101 (2019).

[45]E. G. Hohenstein, N. Luehr, I. S. Ufimtsev, and T. J. Martínez, The Journal of Chemical Physics **142**, 224103 (2015).

[46]N. Luehr, I. S. Ufimtsev, and T. J. Martínez, Journal of Chemical Theory and Computation **7**, 949 (2011).

[47]I. S. Ufimtsev and T. J. Martínez, Journal of Chemical Theory and Computation **4**, 222 (2008).

[48]I. S. Ufimtsev and T. J. Martinez, Journal of Chemical Theory and Computation **5**, 1004 (2009).

[49]J. W. Snyder, E. G. Hohenstein, N. Luehr, and T. J. Martínez, The Journal of Chemical Physics **143**, 154107 (2015).

[50]J. W. Snyder, B. S. Fales, E. G. Hohenstein, B. G. Levine, and T. J. Martínez, The Journal of Chemical Physics **146**, 174113 (2017).

[51]V. Barone and M. Cossi, The Journal of Physical Chemistry A **102**, 1995 (1998).

[52]A. W. Lange and J. M. Herbert, The Journal of Chemical Physics **133**, 244111 (2010).

[53]D. M. York and M. Karplus, The Journal of Physical Chemistry A **103**, 11060 (1999).

[54]F. Liu, D. M. Sanchez, H. J. Kulik, and T. J. Martínez, International Journal of Quantum Chemistry **119**, e25760 (2019).

[55]F. Liu, N. Luehr, H. J. Kulik, and T. J. Martínez, Journal of Chemical Theory and Computation **11**, 3131 (2015).

[56]B. S. Fales and B. G. Levine, Journal of Chemical Theory and Computation **11**, 4708 (2015).

[57]Y.-x. Yuan, Mathematical Programming **151**, 249 (2015).

[58]M. Cossi, V. Barone, and M. A. Robb, The Journal of Chemical Physics **111**, 5295 (1999).

[59]J. STÅLRING, A. BERNHARDSSON, and R. LINDH, Molecular Physics **99**, 103 (2001).

[60]Y. Osamura, Y. Yamaguchi, and H. F. Schaefer, The Journal of Chemical Physics **77**, 383 (1982).

[61]B. H. Lengsfield, P. Saxe, and D. R. Yarkony, The Journal of Chemical Physics **81**, 4549 (1984).

[62]S. Seritan, C. Bannwarth, B. S. Fales, E. G. Hohenstein, S. I. L. Kokkila-Schumacher, N. Luehr, J. W. Snyder, C. Song, A. V. Titov, I. S. Ufimtsev, and T. J. Martínez, The Journal of Chemical Physics **152**, 224110 (2020).

[63]S. Seritan, C. Bannwarth, B. S. Fales, E. G. Hohenstein, C. M. Isborn, S. I. L. Kokkila-Schumacher, X. Li, F. Liu, N. Luehr, J. W. Snyder Jr., C. Song, A. V. Titov, I. S. Ufimtsev, L.-P. Wang, and T. J. Martínez, WIREs Computational Molecular Science **11**, e1494 (2021).

[64]L.-P. Wang and C. Song, The Journal of Chemical Physics **144**, 214108 (2016).

[65]J. Zhang, C. Jiang, J. P. Figueiró Longo, R. B. Azevedo, H. Zhang, and L. A. Muehlmann, Acta Pharmaceutica Sinica B **8**, 137 (2018).

[66]D. A. Kreplin, P. J. Knowles, and H.-J. Werner, The Journal of Chemical Physics **150**, 194106 (2019).

[67]D. A. Kreplin, P. J. Knowles, and H.-J. Werner, The Journal of Chemical Physics **152**, 074102 (2020).

[68]J. W. Park and T. Shiozaki, Molecular Physics **116**, 2583 (2018).

[69]J. Hoche, A. Schulz, L. M. Dietrich, A. Humeniuk, M. Stolte, D. Schmidt, T. Brixner, F. Würthner, and R. Mitric, Chemical Science **10**, 11013 (2019).

[70]L.-P. Wang, R. T. McGibbon, V. S. Pande, and T. J. Martinez, Journal of Chemical Theory and Computation **12**, 638 (2016).

[71]B. Helmich-Paris, Journal of Chemical Theory and Computation **15**, 4170 (2019).

[72]B. Mignolet and B. F. E. Curchod, The Journal of Chemical Physics **148**, 134110 (2018).

[73]M. Ben-Nun, J. Quenneville, and T. J. Martínez, The Journal of Physical Chemistry A **104**, 5161 (2000).

[74]D. S. Sholl and J. C. Tully, The Journal of Chemical Physics **109**, 7702 (1998).

[75]J. C. Tully, International Journal of Quantum Chemistry **40**, 299 (1991).

[76]B. G. Levine and T. J. Martínez, Annual Review of Physical Chemistry **58**, 613 (2007).

[77]M. Zimmer, Chemical Reviews **102**, 759 (2002).

[78]A. Toniolo, S. Olsen, L. Manohar, and T. J. Martínez, Faraday Discussions **127**, 149 (2004).

[79]J. Finley, P.-Å. Malmqvist, B. O. Roos, and L. Serrano-Andrés, Chemical Physics Letters **288**, 299 (1998).

[80]T. Shiozaki, W. Győrffy, P. Celani, and H.-J. Werner, The Journal of Chemical Physics **135**, 081106 (2011).

[81]S. Battaglia and R. Lindh, Journal of Chemical Theory and Computation **16**, 1555 (2020).

[82]S. Battaglia and R. Lindh, The Journal of Chemical Physics **154**, 034102 (2021).

[83]J. W. Snyder, R. M. Parrish, and T. J. Martínez, The Journal of Physical Chemistry Letters **8**, 2432 (2017).

[84]Z. Rinkevicius, X. Li, J. A. R. Sandberg, K. V. Mikkelsen, and H. Ågren, Journal of Chemical Theory and Computation **10**, 989 (2014).

[85]S. M. Morton and L. Jensen, The Journal of Chemical Physics **133**, 074103 (2010).

[86]M. Nottoli, B. Mennucci, and F. Lipparini, Physical Chemistry Chemical Physics **22**, 19532 (2020).